Morphology-Controlled Co_3O_4 Nanoparticles in Boosting Oxygen Reduction and Oxygen Evolution Reactions

In this Chapter, we have investigated the electrocatalytic properties of morphology-controlled Co_3O_4 (nanooctahedron and spongelike) nanoparticles (NPs) anchored on carbon towards ORR and OER in an alkaline media. For comparison, the electrocatalytic activity of carbon (C), polycrystalline Co_3O_4/C (synthesized via hydrothermal method), standard Pt/C (20 Wt.%) and RuO_2 was also studied. The physicochemical and electrochemical properties of the as-prepared ECs were characterized using various analytical techniques. The details of the material synthesis and experimental methodologies are included in the experimental section, Chapter 2.

This chapter is divided into two sections depending on the morphology of Co_3O_4, *i.e.*; carbon supported Co_3O_4 nanooctahedron (Oct-Co_3O_4/C) and sponge-like Co_3O_4 (Sp-Co_3O_4/C).

I. **Section 3A:** Morphology Effect of Co_3O_4 Nanooctahedron in Boosting Oxygen Reduction and Oxygen Evolution Reactions

II. **Section 3B:** Insight into the Structure-Activity Relationship of Sponge-like Structured Co_3O_4/C Electrocatalyst

Morphology Effect of Co_3O_4 Nanooctahedron in Boosting Oxygen Reduction and Oxygen Evolution Reactions

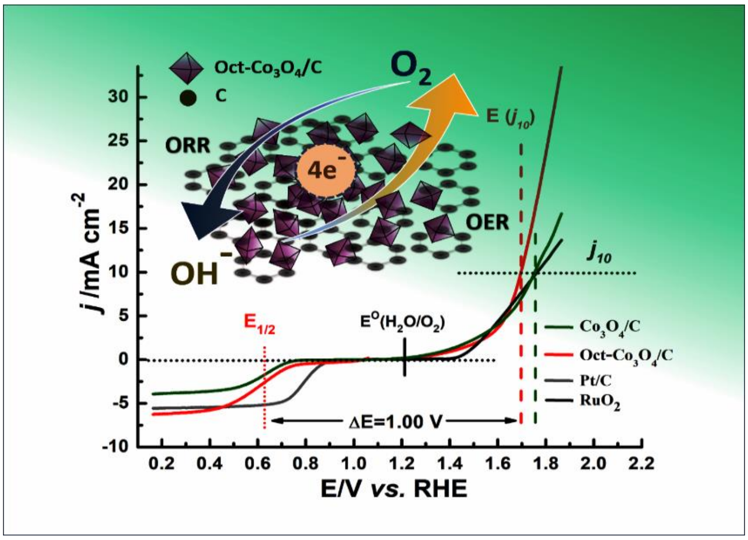

A systematic study on the bifunctional ORR and OER activity exhibited by morphology controlled Co_3O_4 anchored on carbon is explained in this section. This work deals with the synthesis of two different morphology Co_3O_4 i.e., Oct-Co_3O_4/C and polycrystalline-Co_3O_4 by facile two-step solvothermal and hydrothermal synthesis approach respectively, for oxygen electrocatalysis. Oct-Co_3O_4/C possesses rich crystal facets that are predominantly enclosed by (111) planes, which exposes various surface atomic compositions of Co^{2+} and Co^{3+}active sites. It facilitates higher exposed active sites with high BET surface area, ECSA and surface oxygen vacancies. Numerous electrochemical studies establishes that Oct-Co_3O_4/C is a potential non-precious material as a high-performance, durable and stable EC toward ORR and OER in alkaline electrolyte. The experimental and technical details of the synthesis, physicochemical and electrochemical characterization used in this section are discussed in Chapter 2.

---

*The content of this chapter has been published in “ *Energy & Fuels*, 36 (22): 13863–13872, 2022”

3A.1. Introduction

To combat the exponentially growing demand for energy across the globe, the discovery of high-efficiency energy-conversion techniques is of prime urgency. Whilst carbon-based fossil fuels are still serving the purpose, they would soon run down considering the current rate of its depletion. Not to forget that usage of carbon-based fossil-fuel derivatives like petrol and diesel in automobiles emit a lot of greenhouse gases into the open air which we breathe, causing respiratory distress and at the same time, is a major cause of global warming [1-3]. A large portion of the nation's gross domestic income is being put into green-energy research. Electrochemical devices like polymer electrolyte membrane (PEM) FC electrolyzers, MABs, overall water-splitting devices, etc. have a significant contribution in this domain [4,5]. However, due to the various techno-economic challenges, the wide market penetration of fuel cells is still not realized [6]. The two most important oxygen reactions in these electrolyzers, *viz.* ORR/OER exhibit sluggish kinetics and demand high external current [7-9]. By far, standard 20 wt.% Pt/C and RuO_2, are considered as the benchmark ECs for ORR and OER, respectively [10-12]. Nevertheless, these ECs exhibit inferior stability and are coagulation-prone. The major bottleneck of these state-of-the-art ECs is its material cost which makes it impractical for day-to-day utility. According to strategic analysis, the upfront cost of fuel cells is around US \$11.24 kW^{-1} where US \$10 kW^{-1} attributes to Pt usage [13]. Also, these standard catalysts are only monofunctionally active, thereby limiting its complete material utilization. Similarly, for OER, although numerous TMOs have been found to be OER active, RuO_2 remains the most efficient catalyst generating 10 mA cm^{-2} per geometric area with the least overpotential in both aqueous acidic and alkaline media [14]. Hence, despite all their shortcomings, Pt/C and RuO_2 remain the standard benchmarks due to their undeniable efficiency towards ORR and OER, respectively. Hence, the search for bifunctional, affordable, highly efficient and durable oxygen ECs is significantly imperative and at the same time, greatly challenging to achieve.

Non-noble metal oxides, as the class of non-precious materials, are being studied extensively in recent years because of its outstanding response toward oxygen electrocatalysis [15-19]. Co-based ECs have been explored as promising candidates for O_2 electrochemistry. Cobalt being non-noble and earth-abundant, boosted by its multi-state valences (+2/+3) renders it a favourable choice in the oxides and spinel family

[20-23]. Scholarly articles on Ni, Co, Fe, and Mn-based OER date back to more than half a century ago and a lot of these indicate that Co-based oxides/hydroxides possess near optimal M−OH bond strength which is an important descriptor of OER activity [24]. For ORR, Co-based catalysts (like Co_xO_y, Co_xS_y, Co_xSe_y) have attracted the most attention among all other non-PGM electrocatalysts which is evident from the number of published articles in the past few years [25]. Apart from the facile +2/+3 shuttle, the redox potential of metallic Co is very near to 1.23 V vs. RHE which is the potential for ORR [26]. Added enhancement of conductivity and overall electrocatalytic activity is observed from anchoring catalysts onto carbon frameworks [27]. With extensive research, it has been further observed that shape-controlled Co_xO_y-based ECs show dramatical enhancement in electrocatalytic activity compared to pristine Co_xO_y [18,28]. The interplay between particle shape and its catalyst effectiveness is universally acknowledged after numerous DFT simulations as well as experimental proofs [29]. With the difference in synthesis routes, catalysts with different shapes are formed, like cubes, tetrahedrons, octahedrons, cuboctahedrons, and sphere-like structures. This brings substantial differences in their physico-chemical properties, thereby changing their electrochemical response. Crystallographic changes occur with the change in shape which causes rearrangements in *d*-band centre which is an important descriptor of the adsorption energy of a reactant molecule onto a metal surface [30]. The dominant facet differs for different shapes of the same material which makes them vary greatly in their affinity towards a particular reaction. For instance, Wang *et al.* in one of their studies found that Pt nanocubes with (100) facets were more ORR active than Pt polyhedrons and truncated cubes which have (111) facets [31]. Similarly, a detailed study by Xiao *et al.* in 2003 with different shapes of spinel Co_3O_4 shows that the ORR affinity decreases with facets (111) > (100) > (110) [32]. Hence, surface-engineering of spinel Co_3O_4 to synthesize the most active surface towards oxygen electrochemistry is a potential way of enhancing catalytic performance, which is a challenging task at the same time. The oxygen vacancies in MOs are characteristic and intrinsic defects with vibrant impacts on the physico-chemical properties of the electrocatalysts. It has the potential to expose new opportunities for achieving efficient MO catalysts. Usually, the oxygen vacancies can be regulated by the oxygen partial pressure, synthesis temperature and calcination temperature irrespective of any morphological shape and size of the material [33].

However, in the case of shape-controlled MOs, the oxygen vacancies can be readily generated at the region of the predominant and largely exposed polar crystal facets. This attracts us to lay focus on designing shape-controlled catalysts. Whilst a proper surfactant is considered necessary for shape-mediated synthesis [34,35], we report a facile, two-step solvothermal synthesis of Co_3O_4 octahedrons supported upon Vulcan XC72R carbon, named as Oct-Co_3O_4/C. These octahedrons were successfully employed for O_2 electrochemistry in 0.1 M KOH electrolyte as an efficient, highly stable and durable bifunctional oxygen EC. Proper nucleation and controlled growth were able to achieve without the assistance of any shape-mediator.

3A.2. Results and Discussion

3A.2.1.Morphological characterization of the synthesized ECs

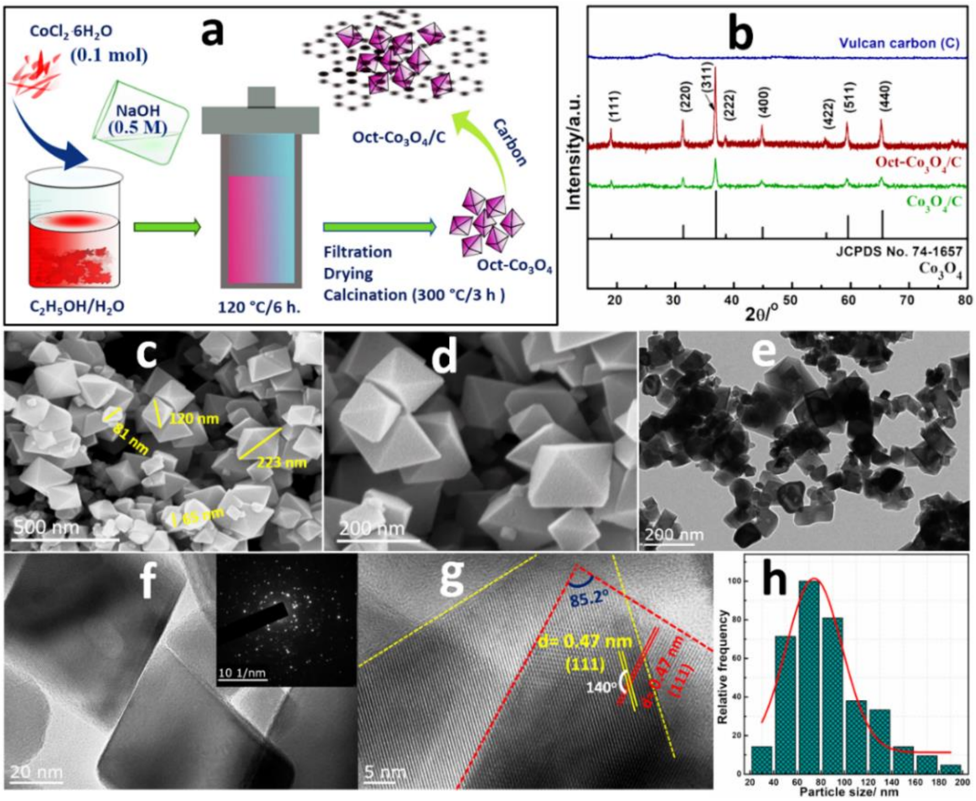

Figure 3A.1. (a) Schematic representation for the synthesis of the Oct-Co_3O_4, (b) XRD patterns of C, Co_3O_4/C and Oct-Co_3O_4/C, (c and d) SEM images Oct-Co_3O_4, (e-g) TEM, HRTEM images and SAED pattern (inset of figure f) of Oct-Co_3O_4 and (h) particle size distribution of Oct-Co_3O_4 (evaluated from the image c).

The synthesis of shape-controlled Oct-Co_3O_4/C EC is illustrated schematically in Figure 3A.1 a. The phase purity and structural properties of the as-synthesized catalysts were examined by XRD analysis. The XRD patterns presented in Figure 3A.1 b show the diffraction peaks for the investigated samples that could be indexed to both Oct-Co_3O_4/C and polycrystalline Co_3O_4/C phase (JCPDS no. 74-1657). Oct-Co_3O_4/C exhibited higher peak intensity compared to that of Co_3O_4/C because of its high crystalline nature. The high crystallinity of Oct-Co_3O_4/C ensures remarkable electrical conductivity [36]. The peaks observed at angles (2θ) 19.1°, 31.3°, 36.9°, 38.6°, 44.9°, 55.8°, 59.5° and 65.4° are due to the crystallographic diffractions of (111), (220), (311), (222), (400), (422), (511) and (440) planes of Oct-Co_3O_4/C and Co_3O_4/C [37]. Vulcan carbon (C) exposes the characteristic graphitic C-sp^2 structure with a broad and weak intensity peak at about $2\theta = 24^o$, which disappears in Oct-Co_3O_4/C, and Co_3O_4/C owing to the poor crystallinity of C [38].

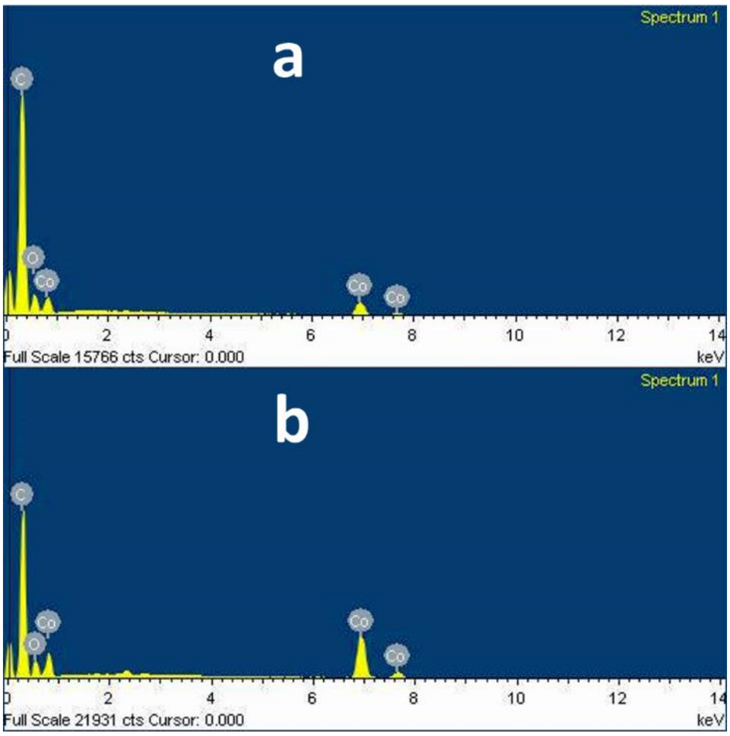

Figure 3A.2. EDX spectra of the ECs. a) Co_3O_4/C and b) Oct-Co_3O_4/C.

The elemental analysis and atomic percentages in Oct-Co_3O_4/C, and Co_3O_4/C were performed by EDX. The atomic percentages of Co, O and C in Oct-Co_3O_4/C were 3.52, 15.24 and 81.24 %, respectively. EDX spectra and percentage compositions of the Oct-Co_3O_4/C, and Co_3O_4/C are summarized in Figure 3A.2 and Table 3A.1, respectively.

Table 3A.1. Physical properties of the as-prepared ECs

Electrocatalysts (ECs)	Element	Wt. % [a]	At. % [a]	BET surface area (m^2/g)	Av. Pore size (nm)
Co_3O_4/C	C	71.74	80.59	123	3.2
	O	21.06	17.76		
	Co	7.20	1.65		
Oct-Co_3O_4/C	C	68.39	81.24	131.3	3.6
	O	17.09	15.24		
	Co	14.53	3.52		

[a] The Wt.% and At.% are evaluated based on EDX measurement.

The particle size and morphological features of Oct-Co_3O_4 were studied with SEM and TEM imaging techniques. The SEM (Figure 3A.1 c, d) and TEM (Figure 3A.1 e, f) images demonstrated the highly crystalline nano-dimensional octahedron shape of as-synthesized Oct-Co_3O_4. The SEM and TEM images further reveal the well-organized homogeneous distribution of the nanooctahedrons. Additionally, the corresponding SAED pattern (inset in Figure 3A.1 f) exposes the clear crystalline structure with the Co_3O_4 phases in different orientations. The HRTEM image in Figure 3A.1 g displays the crystal with the lattice spacing of 0.47 nm, which belongs to the (111) crystal plane of Oct-Co_3O_4. The facets with a lattice spacing of 0.47 nm appear to be distributed in different orientations with various dihedral angles suggesting that the resulting dominant exposed facets are due to the (111) plane [39]. The measured angle between the edges of 85.2°, as observed in Figure 3A.1 g suggests the irregular octahedral shape of Oct-Co_3O_4. The particle size distribution for Oct-Co_3O_4 and presented in Figure 3A.1 h. The average particle size was recognized to be ~ 60-80 nm. The SEM and TEM images of the Co_3O_4 is shown in Figure 3A.3 which suggest the polycrystalline nature of the material in the micro-level dimensions.

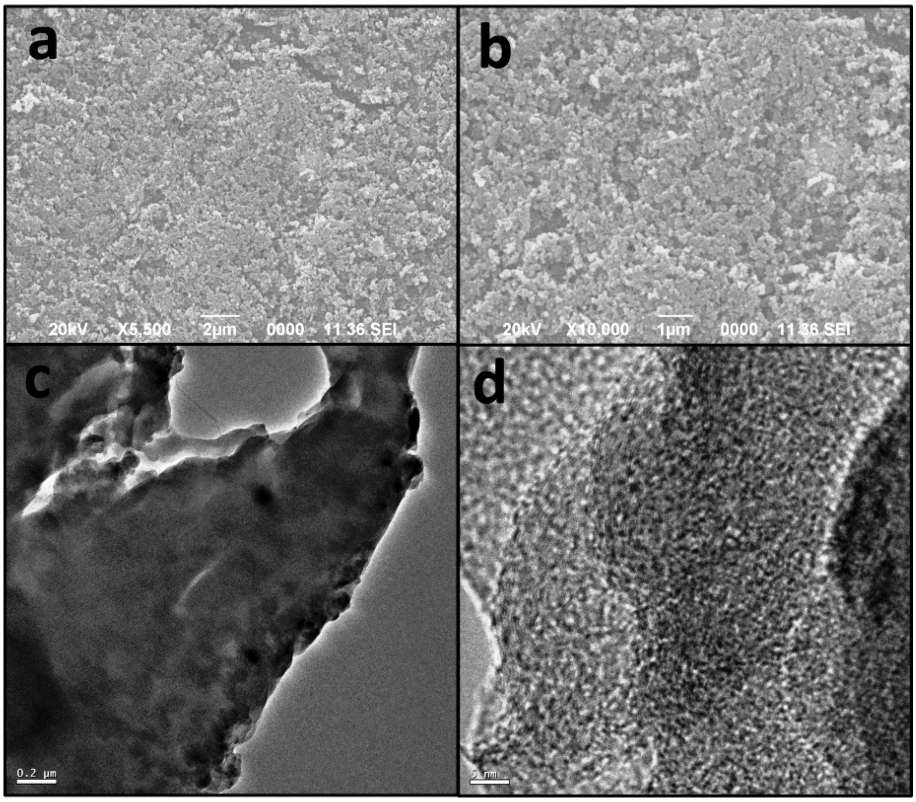

Figure 3A.3. a, b) SEM images of Co_3O_4 and c, d) TEM and HRTEM images of Co_3O_4.

The specific surface area of Co_3O_4/C and Oct-Co_3O_4/C was determined by the BET method. The N_2 adsorption-desorption isotherms of the ECs are shown in Figures 3A.4 a and b. The catalysts possessed the characteristics of type-IV isotherm and H3-type hysteresis loop [40]. The nanoparticulate textural nature attained from the N_2 adsorption/desorption analysis is outlined in Table 3A.1. The calculated specific surface areas for Co_3O_4/C and Oct-Co_3O_4/C are 123 and 131.3 m^2 g^{-1} respectively. The insets of Figure 3A.4 a and b show the corresponding pore size distribution curves, accomplished by the BJH method. The evaluated average pore diameters were 3.2 and 3.6 nm, respectively for Co_3O_4/C and Oct-Co_3O_4/C suggesting the characteristics mesoporous environment of the ECs. The higher BET surface area and mesoporous nature of the Oct-Co_3O_4/C allow the exposure of active sites accommodating the rapid transport of O_2 throughout the courses of electrocatalysis.

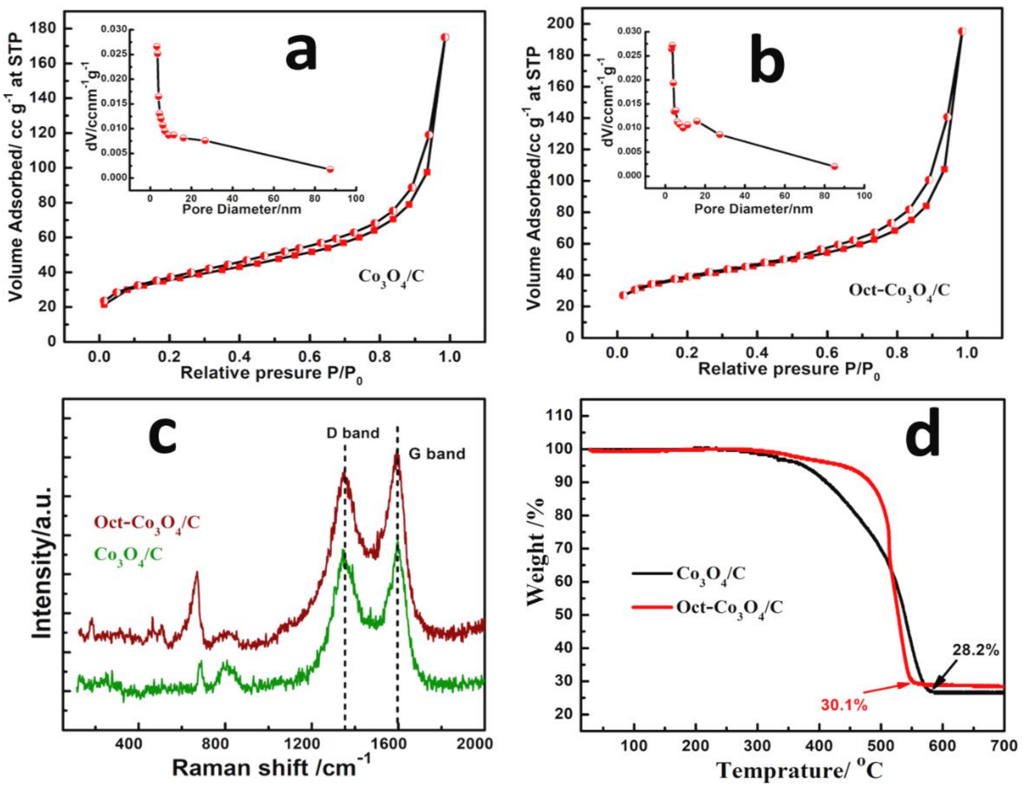

Figure 3A.4. N_2 adsorption-desorption isotherms of (a) Co_3O_4/C and (b) Oct-Co_3O_4/C (corresponding inset: Pore size distribution curve), (c) Raman spectra and (d) TGA profile of the ECs.

Raman spectroscopic analyses were employed to study the characteristic Raman active properties of carbon and Co_3O_4 species. The peak at 1365 cm^{-1} is referred as the D band spectrum arising from the edge or defect sites of carbon whereas the peak at 1595 cm^{-1} is the G band, corresponding to the E_{2g} mode of sp^2-bonded carbon atoms (Figure 3A.4 c) [41,42]. The Raman spectrum of the Oct-Co_3O_4/C in the range of 100–900 cm^{-1} shows four distinct peaks at ∼183, ∼464, ∼507, and ∼670 cm^{-1}, corresponding to the Raman-active modes (F_{2g}, E_g, F_{2g} and A_{1g} symmetry, respectively) of crystalline spinel Co_3O_4, where one Co(II) is located at the tetrahedral site and two Co(III) are localized at the octahedral site with four O^{2-} [43,44]. The Raman peak at ∼670 cm^{-1} is ascribed to the typical A_{1g} octahedral (O_h) sites, whereas the E_g and F_{2g} modes are attributed to the blended motion of the tetrahedral (T_d) site and O_h oxygen vibration [43]. Zhang *et al.* reported that Co–Co interactions at the proximity of O_h edges of its spinel framework directly stimulate the ORR activity via enhanced electronic conductivity [42]. It is noteworthy that the relative intensity of the Raman peaks for Co_3O_4/C is significantly lower as compared to that of Oct-Co_3O_4/C peaks which is due to the lower crystallinity of Co_3O_4/C. The relatively higher peak intensity and the significant negative shift of the A_{1g} mode in Oct-Co_3O_4/C reveal the creation of more surface oxygen vacancies which is further attributed to the size and shape effects of the EC [45]. The Co_3O_4 wt.% of the ECs were evaluated from TGA analyses. Figure 3A.4 d shows the TGA curves of the ECs which illustrate the decay of carbon components with increasing temperature. With the increase in temperature, the sample losses its mass (~70 wt.%) which is because of the oxidation of carbon to CO_2 and the plots get stable at ~ 550 °C suggesting the residual ~30 wt.% is the Co_3O_4 content in the ECs.

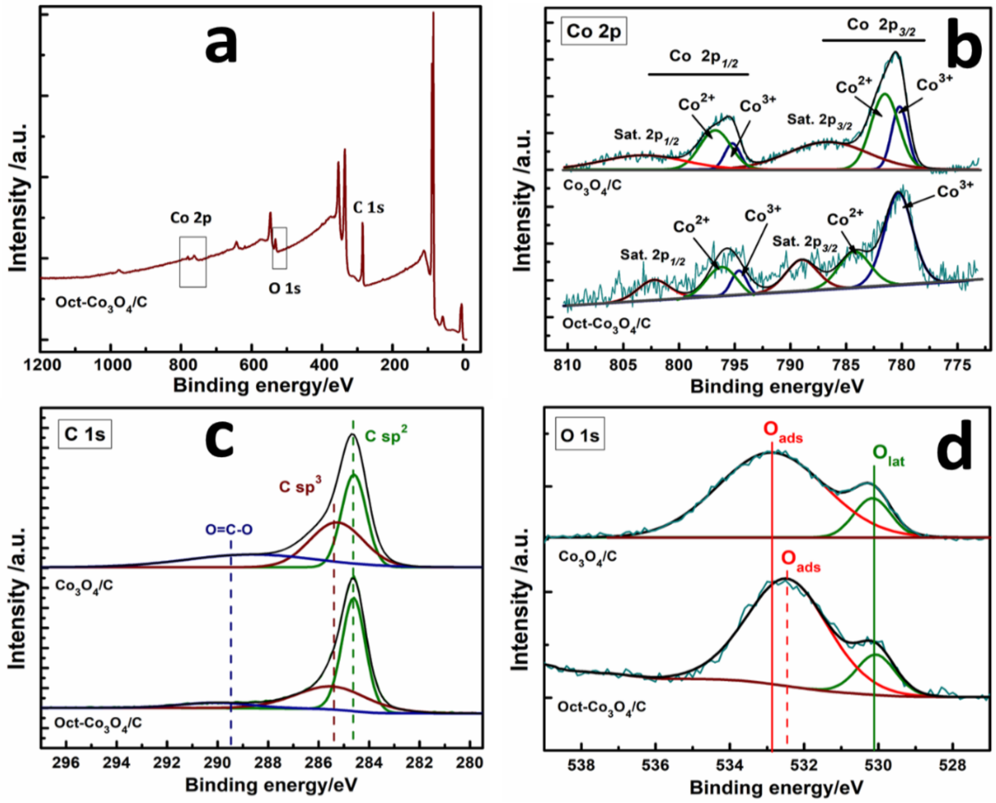

Figure 3A.5. a) XPS survey spectrum of Oct-Co_3O_4/C; Core-level XPS spectrum of b) Co 2p, c) O 1s and d) C 1s for Oct-Co_3O_4/C and Co_3O_4/C.

Further insight into the surface chemical compositions and metal oxidation states of the ECs are explored using XPS analysis. The XPS spectra of the metal species, surface oxygen and carbon along with the survey spectrum of Oct-Co_3O_4/C are shown in Figure 3A.5 which is calibrated with a C 1s peak of 284.6 eV. The XPS survey spectrum (Figure 3A.5 a) shows the relative intensity and peak position in binding energy (BE) of only detectable elements C (1s), O (1s) and Co (2p) signifying the high purity of the sample. The core-level Co 2p spectrum for Oct-Co_3O_4/C and

Co_3O_4/C (Figure 3A.5 b) exhibit a low energy and a high energy band at 780.4 and 795.6 eV separated by spin-orbit splitting energy of 15 eV, corresponding to Co $2p_{3/2}$ and Co $2p_{1/2}$, with two satellite peaks at 788.9 eV and 802.3 eV. These peaks are characteristic of Co_3O_4 [47]. The peaks with the BE of 780.4 and 795.6 eV are attributed to Co^{3+} that it is confined in O_h oxygen coordination and shows a satellite peak at 8.5 eV above the main $2p_{3/2}$ peak, whereas the peak at 795.6 eV is ascribed to Co^{2+} with T_d coordination and shows a satellite peak at 6.7 eV above the main $2p_{1/2}$ peak. The Co^{2+}/Co^{3+} ratio is a qualitative descriptor of surface oxygen vacancy that specifies the availability of defective sites in Oct-Co_3O_4. The Co^{2+}/Co^{3+} ratios has been calculated from the cumulative peak area of the deconvoluted peaks of the respective ions. The Co^{2+}/Co^{3+} ratio for Oct-Co_3O_4 is 0.28 which confirms the presence of oxygen vacancy in the EC, while the Co^{2+}/Co^{3+} ratio for Co_3O_4 is observed to be 2.31 suggesting the presence of a smaller number of Co^{3+} active center in comparison to that of Co^{2+}. The deconvoluted O 1s spectrum as displayed in Figure 3A.5 c display two peaks at 529.8 and 532.3 eV, suggesting the lattice oxygen (O_{lat}) which is the characteristic of metal-oxygen bonding interaction in the spinel and adsorbed oxygen (O_{ads}) on the surface Oct-Co_3O_4/C respectively [47]. The deconvolution of C 1s XPS spectrum reveals the chemical state of C in Oct-Co_3O_4/C (Figure 3A.5 d). The sp^2-C in C 1s peak signifies the population of graphitic C in the catalyst [48].

3A.2.2. Electrocatalytic Activity

The ORR performance of as-prepared ECs was analyzed by applying the CV and RDE electroanalytical method in a 0.1 M KOH solution. Figure 3A.6 show the CV curves measured in N_2 (dotted lines) and O_2 (solid lines) saturated 0.1 M KOH. The characteristics reduction peaks detected in the CVs in O_2 saturated 0.1 M KOH indicate the ORR active nature of the as-prepared ECs. The ORR onset potential (E_{onset}) exhibited by C and Co_3O_4/C is 0.75 and 0.79 V (vs. RHE) respectively whereas for Oct-Co_3O_4/C, which predominantly exposes (111) surfaces, it is achieved to be 0.89 V, signifying a superior positive E_{onset} catalyzed by Oct-Co_3O_4/C. In addition, the higher CV curve area exhibited by Oct-Co_3O_4/C compared to C and Co_3O_4/C suggests a high surface area coupled with the EC. The ORR kinetics evaluated from the LSV curves studied through RDE measurements are shown in Figures 3A.6 b and c. The E_{onset} trends of the ECs observed from the LSV curves are comparable with the CV study.

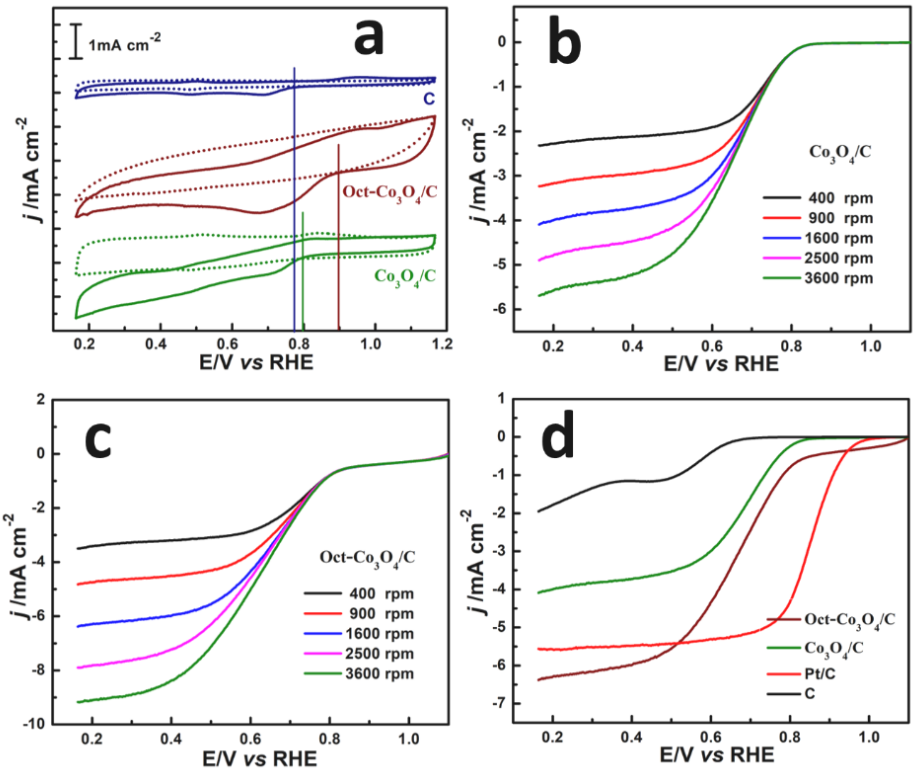

Figure 3A.6. ORR performance of the ECs: a) CVs of C, Oct-Co_3O_4/C and Co_3O_4/C in N_2 and O_2 -saturated 0.1 M KOH, b, c) LSV curves of Co_3O_4/C and Oct-Co_3O_4/C, at various rotations respectively, d) limiting current density comparison of C, Pt/C, Oct-Co_3O_4/C and Co_3O_4/C at 1600 rpm.

Figure 3A.6 d portrays the LSV plots representing the current densities and E_{onset} for C, Pt/C, Oct-Co_3O_4/C and Co_3O_4/C at 1600 rpm. The limiting current density (*j*) of Oct-Co_3O_4/C is – 6.38 mA cm^{-2} which is superior to that of C (−1.9 mA cm^{-2}) and Co_3O_4/C (−4.09 mA cm^{-2}) and commercial Pt/C (−5.50 mA cm^{-2}). The half-wave potential ($E_{1/2}$) is evaluated to be 0.60, 0.84, 0.68 and 0.67 V, respectively for C, Pt/C, Oct-Co_3O_4/C and Co_3O_4/C.

The number of electrons (n) involved in an elementary ORR route is a crucial consideration that determines the ORR efficiency. The ‘n’ value is evaluated based on Koutecky−Levich (K−L) equation [49]. K-L plots of the studied ECs at 0.40 V is presented in Figure 3A.7 a, which demonstrates the ‘n’ values for Oct-Co_3O_4/C and Co_3O_4/C Pt/C and C are 4, 3.2, 4 and 2.8, respectively suggesting that the Oct-Co_3O_4/C and Pt/C proceed through a direct $4e^-$ ORR route without developing an

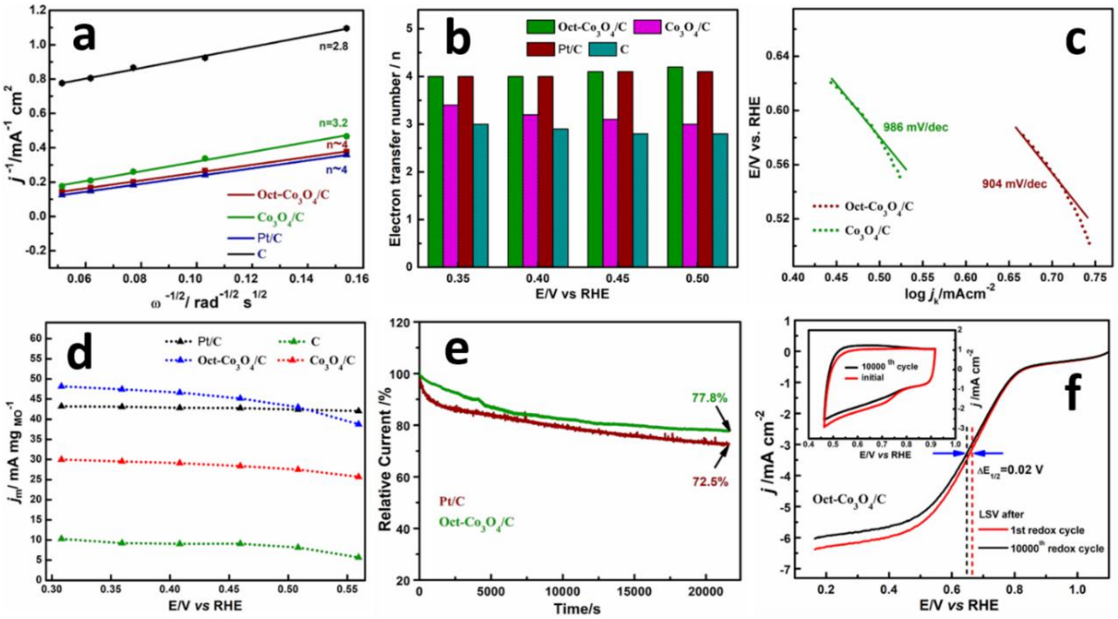

Figure 3A.7. a) K-L plots of C, Pt/C, Oct-Co_3O_4/C and Co_3O_4/C at 0.40 V, b) number of electrons transferred during ORR at various potentials for different ECs, c) Tafel plots of Oct-Co_3O_4/C and Co_3O_4/C, d) mass-specific activity (MA) at 1600 rpm. e) chronoamperometric test for Oct-Co_3O_4/C and Pt/C and f) accelerated durability test for Oct-Co_3O_4/C.

intermediate product (H_2O_2) whereas Co_3O_4/C and C facilitate an indirect ORR pathway. The parallel fitting lines of the K−L slope indicate first-order ORR kinetics in the catalysis process. In addition, the 'n' values were calculated over a broad potential range as presented in Figure 3A.7 b displays a consistent $4e^-$ pathway unveiled by Oct-Co_3O_4/C. The reaction kinetics of ORR catalyzed by Oct-Co_3O_4/C and Co_3O_4/C is further studied with the Tafel slope (Figure 3A.7 c) in the mixed kinetic-diffusion controlled region. Oct-Co_3O_4/C shows faster ORR kinetics with a lower Tafel slope (904 mV dec^{-1}) in comparison to that of Co_3O_4/C (986 mV dec^{-1}). The mass activity (MA) for the investigated ECs in the potential range of 0.30-0.55 V is evaluated and shown in Figure 3A.7 d. The trends in MA for the set of inspected ECs follow the order Oct-Co_3O_4/C >Pt/C >Co_3O_4/C >C which portrays the characteristic intrinsic ORR activity of the ECs. To assess the catalytic stability and durability of Oct-Co_3O_4/C chronoamperometric (CA) test is performed. Figure 3A.7 e displays the CA activity of Oct-Co_3O_4/C accomplished up to 6 h, which is further compared with the CA activity of Pt/C. Oct-Co_3O_4/C shows higher retention of its initial current (77.8%) while Pt/C shows 72.5% of its initial current, after 6 h of CA operations. The catalytic stability and durability of Oct-Co_3O_4/C are further studied with the accelerated durability test. The comparison of the initial and the final ORR polarization curves after the operation of 10000 redox cycles is shown in Figure 3A.7 f. The observed Δj (0.35 mA cm^{-2}) and $\Delta E_{1/2}$ (0.02 V) are significantly smaller after the 10000 redox cycle, suggesting the excellent stability and durability exhibited by the catalyst Oct-Co_3O_4/C.

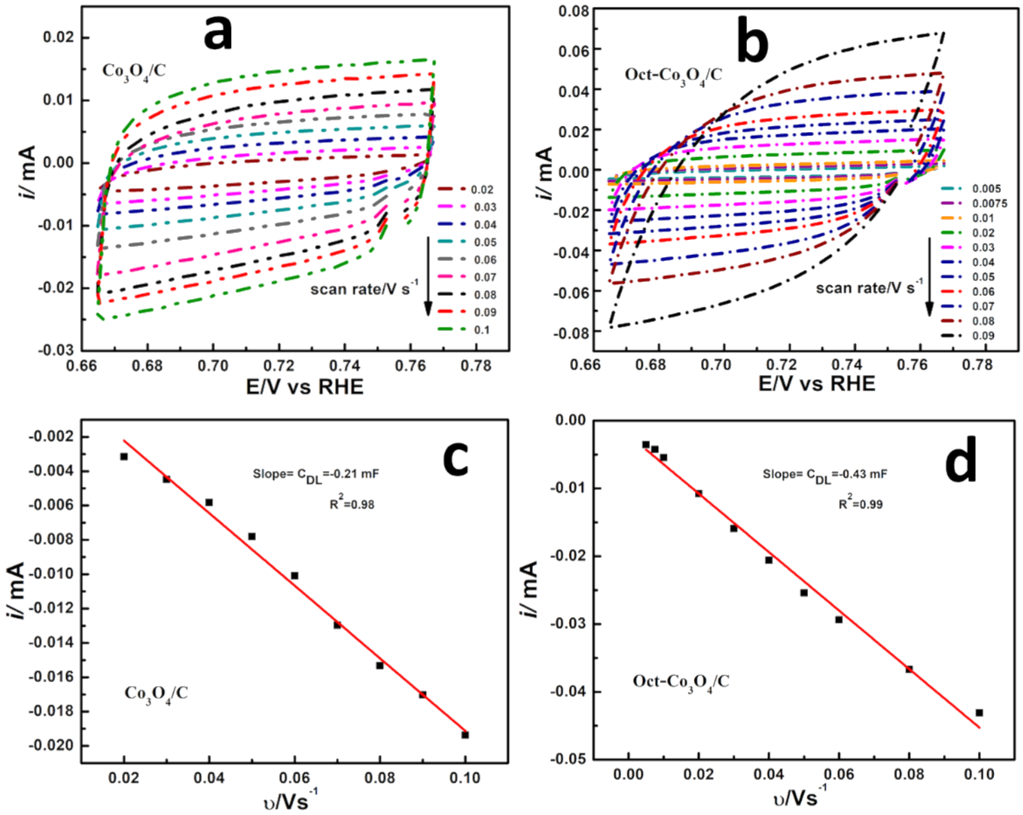

Figure 3A.8. C_{dl} measurements for determining ECSA in 0.1 M KOH. a,b) CVs of Co_3O_4/C and Oct-Co_3O_4/C at various scan rates. c,d) The slope of scan rate vs current obtained from the respective CV data.

The ECSA of the ECs is assessed from the CV-derived double-layer capacitance (C_{dl}) in an N_2-saturated 0.1 M KOH solution. Figure 3A.8 a and b display the scan rate-dependent CV curves of Co_3O_4/C and Oct-Co_3O_4/C assessed in the non-Faradaic region. The slope of the plot of cathodic current vs. the scan rate expresses the C_{dl} value for the ECs as shown in Figure 3A.8 c and d. The corresponding ECSA for Co_3O_4/C and Oct-Co_3O_4/C are 17.50 and 35.83 $m^2\ g^{-1}$ respectively, demonstrating the availability of more active sites in the Oct-Co_3O_4/C. The higher ECSA of the Oct-

Co_3O_4/C can be ascribed to the characteristic synergy between the well-shaped morphology-assisted Co_3O_4 and the carbon support.

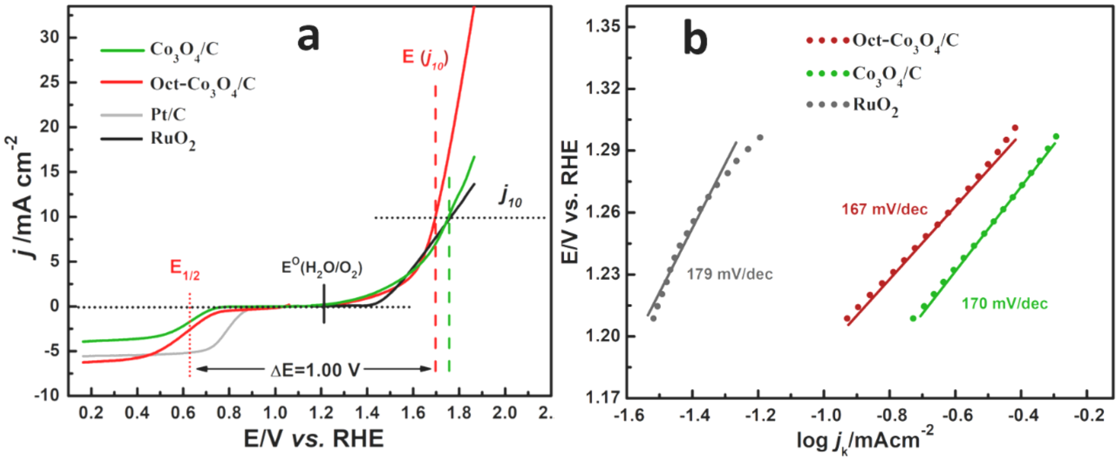

Figure 3A.9. a) Bifunctional (ORR/OER) activities of Oct-Co_3O_4/C compared with Pt/C, RuO_2 and Co_3O_4/C, b) OER Tafel plots for Oct-Co_3O_4/C, Co_3O_4/C and RuO_2.

Besides ORR, the OER performance of Oct-Co_3O_4/C is evaluated which is further compared with the Co_3O_4/C and the commercial RuO_2. The current density of 10 mA cm^{-2} (j_{10}) for OER is the average current density for 10% energy conversion in a water-splitting device which can be regarded as a baseline parameter to evaluate OER efficiency [49]. Figure 3A.9 a, shows the overall bifunctional (ORR/OER) activities exhibited by the investigated ECs. It is observed that for OER, Oct-Co_3O_4/C achieves 10 mA cm^{-2} at an overpotential (η_{10}) of 0.45 V, which is 70 mV lower than that of Co_3O_4/C (η_{10}=0.52 V) and 80 mV lower than the benchmark RuO_2 (η_{10}=0.53 V) suggesting the OER superiority of Oct-Co_3O_4/C. The potentials at j_{10} i.e., E_{j10} values for Co_3O_4/C, Oct-Co_3O_4/C and RuO_2 are observed as 1.75, 1.68 and 1.76 V, respectively. The reversibility index was evaluated by the variance of OER and ORR metrics: $\Delta E = E_{j10} - E_{1/2}$ [49,50]. A smaller ΔE value is appreciated for the efficient bifunctional performance as the reversibility is more feasible with the low value of ΔE. Oct-Co_3O_4/C demonstrated a smaller ΔE value (1.00 V) than that of Co_3O_4/C (1.08), which is comparable to the noble-metal benchmarks Pt/C and RuO_2 and previously reported bifunctional ECs Co-NC 750 ($\Delta E = 1.02$ V) [51], Co_3O_4-CeO_2/C ($\Delta E = 1.04$ V) [52], Co_3O_4/2.7Co_2MnO_4 ($\Delta E = 1.09$ V) [53] signifying the superior bifunctional performance of Oct-Co_3O_4/C for ORR and OER. The OER kinetics of the ECs is analyzed by OER Tafel plots. Figure 3A.9.b portrays that the Oct-Co_3O_4/C displays the lowest Tafel slope of 167 mV dec^{-1} in the lower overpotential region than that of Co_3O_4/C (170 mV dec^{-1}) and RuO_2 (179 mV dec^{-1}), signifying that Oct-Co_3O_4/C catalyzes with faster oxygen evolution rate at the electrode surface.

ΔE along with other electrochemical parameters such as E_{onset}, $E_{1/2}$, *j*, and overpotential for the OER (E_{j10}) are demonstrated in comparison to the recently reported works as shown in Table 3A.2. For assessing the electrocatalytic performance the onset potential is a key parameter. As displayed in Figure 3A.6 a, the Oct-Co_3O_4/C exhibited ORR E_{onset} of 0.89 V, which is superior and comparable to most of the reported Co-oxide based ECs, such as, Co_3O_4-NC/N-rGO (E_{onset}= 0.82), Co_3O_4-NTO/N-rGO (E_{onset}=0.84), Co_3O_4-NP/N-rGO(E_{onset}=0.89), Co-NC 750 (E_{onset}=0.87), Co/$CoFe_2O_4$ (E_{onset}=0.77) and Co_3O_4-CeO_2/C (E_{onset}=0.84). Correspondingly, when it comes to the limiting current density (*j*), Oct-Co_3O_4/C exhibited *j*= –6.38 mA cm^{-2} outperforming the activity possessed by reported Co-oxide-based ECs as shown in Table 3A.2. The overall bifunctional electrocatalytic activities of Oct-Co_3O_4/C (including ORR/OER E_{onset}, $E_{1/2}$, *j*, E_{j10} and ΔE) are reasonable to the recently reported ECs.

The excellent ORR/OER bifunctional activity of the Oct-Co_3O_4/C can be enlightened with the morphology-based structure-activity relationship. Oct-Co_3O_4/C possesses the rich crystal facets that are predominantly enclosed by (111) planes as revealed from the HRTEM images, which exposes various surface atomic compositions of Co^{2+} and Co^{3+}active sites. Based on the experimental and theoretical simulation analyses it is reported that the surface atomic configuration of Co^{2+}/Co^{3+} active sites, particularly the availability of octahedrally coordinated Co^{3+} sites (Co^{3+}_{Oh}), synchronises the adsorption, activation, and desorption properties of the molecular oxygen that correlates with the diverse electrocatalytic behaviour of different facets enfolded Co_3O_4 NPs [56]. For instance, Xiao et al demonstrated a morphology-controlled synthesis of Co_3O_4 with the various exposed crystalline surfaces (nanorods-(110), nanocubes-(100) etc.) supported on graphene sheets to study the effects of the active surface structure toward ORR and the electrocatalytic activity is reported to be intimately associated with the extent of the catalytically active sites i.e., Co^{2+}/Co^{3+} [32].

Table 3A.2. ORR/OER performance of recently reported Co-oxide-based ECs in 0.1 M KOH Solution*.

ECs	**ORR**			**OER**		**ΔE/V** [E(j_{10})–$E_{1/2}$)]	**Ref.**
	E_{onset} /V	$E_{1/2}$/V	j/ mA cm^{-2}	E(j_{10})/ V	E_{onset}/ V		
Co-NC 750	0.87	0.78	~ –5.40	1.80	1.58	1.02	[51]
Co_3O_4-CeO_2/C	0.84	0.69	–4.20	1.73	1.20	1.04	[52]
Co_3O_4/2.7Co_2MnO_4	--	0.68	--	1.77	--	1.09	[53]
Co_3O_4/CNF	0.92	0.85	–0.38	1.65	--	0.80	[54]
CoO-Co/CNF	0.92	0.86	–0.29	1.67	--	0.81	[55]
Co_3O_4-NC/N-rGO	0.82	0.68	–4.98	1.67	~ 1.62	0.99	[56]
Co_3O_4-NTO/N-rGO	0.84	0.71	–4.95	1.64	~ 1.61	0.93	[56]
Co_3O_4-NP/N-rGO	0.89	0.76	–5.50	1.61	~ 1.57	0.85	[56]
Co/$CoFe_2O_4$	0.77	0.63	~ –4.40	1.62	--	0.99	[57]
Co_3O_4/C	0.79	0.67	–4.09	1.76	1.26	1.08	This work
Oct-Co_3O_4/C	0.89	0.68	–6.38	1.68	1.26	1.00	This work

*The potentials in an Ag/AgCl electrode were represented in terms of RHE employing the co-relation: $E_{RHE} = E_{Ag/AgCl} + E^{o}_{Ag/AgCl} + 0.059$ pH (pH of 0.1M KOH = 13), where E_{RHE} is the reversible hydrogen electrode potential, $E_{Ag/AgCl}$ is Ag/AgCl electrode potential and $E^{o}_{Ag/AgCl} = 0.1976$ at 25 °C.

The spinel Co_3O_4 nanooctahedrons and oxide/carbon interfaces in Oct-Co_3O_4/C demonstrate significant properties in support of higher exposed active sites (as evident from BET surface area and ECSA, strong electronic coupling effects between Co^{2+} and Co^{3+} and rapid charge interchangeability of $Co^{2+/3+}$ with the adsorbed molecular O_2 [58]. The more surface oxygen vacancies on the Oct-Co_3O_4/C could assist the activation of adsorbed O_2 owing to the enhanced redox ability of the EC [58,59]. In addition, the surface oxygen vacancies could uplift the surface O_2 mobility thereby boosting the O_2 adsorption/desorption which is anticipated for ORR/OER bifunctional activities. The synchronized Co^{2+} in Oct-Co_3O_4/C preferentially act as the active sites for the ORR, on the contrary Co^{3+} favourably initiate the OER process facilitating the overall bifunctional performance [60,61].

3A.3. Conclusions

We developed a facile two-step solvothermal scheme to fabricate Co_3O_4 nanooctahedron anchored on carbon support (Oct-Co_3O_4/C) as a highly efficient, non-precious bifunctional EC for ORR and OER in an alkaline medium. Oct-Co_3O_4/C exhibits ORR/OER activities superior to that of the C, Co_3O_4/C, standard Pt/C (for ORR) and RuO_2 (for OER) corresponding to '*j*' value at significantly lower overpotential with long-term durability and stability. The ORR in Oct-Co_3O_4/C exclusively proceeds through the direct $4e^-$ reduction pathway. Oct-Co_3O_4/C displays a more positive $E_{1/2}$ value than that of the inspected ECs which is reasonable to that of Pt/C. The ORR/OER Tafel plot demonstrated the faster kinetics of Oct-Co_3O_4/C as compared to that of Co_3O_4/C and RuO_2. This is ascribed to the unification and synergistic coupling of highly ordered octahedral Co_3O_4 with Vulcan carbon in conjugation with the high electrical conductivity, high specific surface area and high ECSA of the resulting Oct-Co_3O_4/C. This extensive work presents a highly aspiring ORR/OER EC for alkaline fuel cells with high efficiency, stability, and durability as an alternative to noble metal-based ECs.

References

[1] Asif, M., and Muneer, T. Energy supply, its demand and security issues for developed and emerging economies. *Renewable and Sustainable Energy Reviews*, 11(7):1388-1413, 2007.

[2] Shafiee, S., and Topal, E. When will fossil fuel reserves be diminished? *Energy Policy*, 37(1):181-189, 2009.

[3] Yang, Z.X., Li, X.G., Yao, Q.L., Lu, Z.H., Zhang, N., Xia, J., Yang, K., Wang, Y.Q., Zhang, K., Liu, H.Z., and Zhang, L.T. 2022 roadmap on hydrogen energy from production to utilizations. *Rare Metal*, 41:3251–3267, 2022.

[4] Smith, W. The role of fuel cells in energy storage. *Journal of Power Sources*, 86(1-2):74-83, 2000.

[5] Wang, Y., Chu, F., Zeng, J., Wang, Q., Naren, T., Li, Y., Cheng, Y., Lei, Y. and Wu, F. Single atom catalysts for fuel cells and rechargeable batteries: Principles, advances, and opportunities. *ACS Nano*, 15(1):210-239, 2021.

[6] Wang, J., Wang, H., and Fan, Y. Techno-economic challenges of fuel cell commercialization. *Engineering*, 4(3):352-360, 2018.

[7] Chen, W., Huang, J., Wei, J., Zhou, D., Cai, J., He, Z. D., and Chen, Y. X. Origins of high onset overpotential of oxygen reduction reaction at Pt-based electrocatalysts: A mini review. *Electrochemistry Communications*, 96:71-76, 2018.

[8] Gewirth, A. A., and Thorum, M. S. Electroreduction of dioxygen for fuel-cell applications: Materials and challenges. *Inorganic Chemistry,* 49(8):3557-3566, 2010.

[9] Tahir, M., Pan, L., Idrees, F., Zhang, X., Wang, L., Zou, J. J., and Wang, Z. L. Electrocatalytic oxygen evolution reaction for energy conversion and storage: A comprehensive review. *Nano Energy*, 37:136-157, 2017.

[10] Wu, J., and Yang, H. Platinum-based oxygen reduction electrocatalysts. *Accounts of Chemical Research*, 46(8):1848-1857, 2013.

[11] Suen, N. T., Hung, S. F., Quan, Q., Zhang, N., Xu, Y. J., and Chen, H. M. Electrocatalysis for the oxygen evolution reaction: Recent development and future perspectives. *Chemical Society Reviews*, 46(2):337-365, 2017.

[12] Shi, J., Qiu, F., Yuan, W., Guo, M., and Lu, Z. H. Nitrogen-doped carbon-decorated yolk-shell CoP@FeCoP micro-polyhedra derived from MOF for efficient overall water splitting. *Chemical Engineering Journal*, 403:126312, 2021.

[13] Wang, X., Li, Z., Qu, Y., Yuan, T., Wang, W., Wu, Y., and Li, Y. Review of metal catalysts for oxygen reduction reaction: From nanoscale engineering to atomic design. *Chem*, 5(6):1486-1511, 2019.

[14] McCrory, C. C., Jung, S., Ferrer, I. M., Chatman, S. M., Peters, J. C., and Jaramillo, T. F. Benchmarking hydrogen evolving reaction and oxygen evolving reaction electrocatalysts for solar water splitting devices. *Journal of the American Chemical Society*, 137(13):4347-4357, 2015.

[15] Zhuang, S., Shi, X., and Lee, E. S. A Review on non-PGM cathode catalysts for polymer electrolyte eembrane (PEM) fuel cell. *ASME 2015 13th Int. Conf. Fuel Cell Sci. Eng. Technol. FUELCELL 2015, collocated with ASME 2015 Power Conf. ASME 2015 9th Int. Conf. Energy Sustain. ASME 2015 Nucl. Forum* 2015, 1–11.

[16] Chutia, B., and Bharali, P. Oxygen deficient interfacial effect in CeO_2-modified Fe_2O_3/C for oxygen reduction reaction in alkaline electrolyte. *Catalysis Communications*, 164:106432, 2022.

[17] Patowary, S., Chetry, R., Goswami, C., Chutia, B., and Bharali, P. Oxygen reduction reaction catalysed by supported nanoparticles: Advancements and challenges. *ChemCatChem*, 14(7):e202101472, 2022.

[18] Béjar, J., Álvarez-Contreras, L., Ledesma-García, J., Arjona, N., and Arriaga, L. G. Electrocatalytic evaluation of Co_3O_4 and $NiCo_2O_4$ rosettes-like hierarchical spinel as bifunctional materials for oxygen evolution (OER) and reduction (ORR) reactions in alkaline media. *Journal of Electroanalytical Chemistry*, 847:113190, 2019.

[19] Qiu, F., Shi, J., Guo, M., Chen, S., Xia, J., and Lu, Z. H. Rapid synthesis of large-size Fe_2O_3 nanoparticle decorated NiO nanosheets via electrochemical exfoliation for enhanced oxygen evolution electrocatalysis. *Inorganic Chemistry*, 60(2):959-966, 2020.

[20] Li, B., Zhang, Y., Du, R., Liu, L., and Yu, X. Controllable synthesis of Co3O4 nanocrystals as efficient catalysts for oxygen reduction reaction. *Nanotechnology*, 29(10):105401, 2018.

[21] Huang, J., Sheng, H., Ross, R. D., Han, J., Wang, X., Song, B., and Jin, S. Modifying redox properties and local bonding of Co_3O_4 by CeO_2 enhances oxygen evolution catalysis in acid. *Nature Communications*, 12(1):1-11, 2021.

[22] Alhakemy, A. Z., Senthilkumar, N., Ding, Y., Li, J., and Wen, Z. Co_3O_4–C@FeMoP on nickel foam as bifunctional electrocatalytic electrode for high-performance alkaline water splitting. *International Journal of Hydrogen Energy*, 46(65):32846-32857, 2021.

[23] Wang, Q., Hu, W., and Huang, Y. Nitrogen doped graphene anchored cobalt oxides efficiently bi-functionally catalyze both oxygen reduction reaction and oxygen evolution reaction. *International Journal of Hydrogen Energy*, 42(9):5899-5907, 2017.

[24] Morales-Guio, C. G., Liardet, L., and Hu, X. Oxidatively electrodeposited thin-film transition metal (oxy) hydroxides as oxygen evolution catalysts. *Journal of the American Chemical Society*, 138(28):8946-8957, 2016.

[25] Zhong, H., Gong, X., Zhang, S., Tang, P., Li, D., and Feng, Y. Design and synthesis of cobalt-based electrocatalysts for oxygen reduction reaction. *The Chemical Record*, 18(7-8):840-848, 2018.

[26] Feng, Y., and Alonso-Vante, N. Nonprecious metal catalysts for the molecular oxygen-reduction reaction. *physica status solidi (b)*, 245(9):1792-1806, 2008.

[27] Liang, Y., Li, Y., Wang, H., Zhou, J., Wang, J., Regier, T., and Dai, H. Co_3O_4 nanocrystals on graphene as a synergistic catalyst for oxygen reduction reaction. *Nature Materials*, 10(10):780-786, 2011.

[28] Saddeler, S., Hagemann, U., and Schulz, S. Effect of the size and shape on the electrocatalytic activity of Co_3O_4 nanoparticles in the oxygen evolution reaction. *Inorganic Chemistry*, 59(14):10013-10024, 2020.

[29] Mandić, M., Todić, B., Živanić, L., Nikačević, N., and Bukur, D. B. Effects of catalyst activity, particle size and shape, and process conditions on catalyst effectiveness and methane selectivity for Fischer–Tropsch reaction: a modeling study. *Industrial & Engineering Chemistry Research*, 56(10):2733-2745, 2017.

[30] Cao, S., Tao, F. F., Tang, Y., Li, Y., and Yu, J. Size-and shape-dependent catalytic performances of oxidation and reduction reactions on nanocatalysts. *Chemical Society Reviews*, 45(17):4747-4765, 2016.

[31] Wang, C., Daimon, H., Onodera, T., Koda, T., and Sun, S. A general approach to the size-and shape-controlled synthesis of platinum nanoparticles and their catalytic reduction of oxygen. *Angewandte Chemie International Edition*, 47:3588 –3591,2008.

[32] Xiao, J., Kuang, Q., Yang, S., Xiao, F., Wang, S., and Guo, L. Surface structure dependent electrocatalytic activity of Co_3O_4 anchored on graphene sheets toward oxygen reduction reaction. *Scientific Reports*, 3(1):2300, 2013.

[33] Zhao, P., Qin, F., Huang, Z., Sun, C., Shen, W., and Xu, H. Morphology-dependent oxygen vacancies and synergistic effects of Ni/CeO_2 catalysts for N_2O decomposition. *Catalysis Science & Technology*, 8(1):276-288, 2018.

[34] Xiao, J., and Qi, L. Surfactant-assisted, shape-controlled synthesis of gold nanocrystals. *Nanoscale*, 3(4):1383-1396, 2011.

[35] An, K., and Somorjai, G. A. Size and shape control of metal nanoparticles for reaction selectivity in catalysis. *ChemCatChem*, 4(10):1512-1524, 2012.

[36] Li, X., You, S., Du, J., Dai, Y., Chen, H., Cai, Z., Ren, N. and Zou, J. ZIF-67-derived Co_3O_4@ carbon protected by oxygen-buffering CeO_2 as an efficient catalyst for boosting oxygen reduction/evolution reactions. *Journal of Materials Chemistry A*, 7(45):25853-25864, 2019.

[37] Lin, Q., Liu, B., Jiang, F., Fang, X., Xu, Y., and Liu, X. Assessing the formation of cobalt carbide and its catalytic performance under realistic reaction conditions

and tuning product selectivity in a cobalt-based FTS reaction. *Catalysis Science & Technology*, 9(12):3238-3258, 2019.

[38] Chutia, B., Hussain, N., Puzari, P., Jampaiah, D., Bhargava, S. K., Matus, E. V., Ismagilov, I.Z., Kerzhentsev, M. and Bharali, P. Unraveling the role of CeO_2 in stabilization of multivalent Mn species on α-MnO_2/Mn_3O_4/CeO_2/C surface for enhanced electrocatalysis. *Energy & Fuels*, 35(13):10756-10769, 2021.

[39] Tian, Y., Cao, L., and Qin, P. Bimetal–organic framework derived high‐valence‐state Cu-doped Co_3O_4 porous nanosheet arrays for efficient oxygen evolution and water splitting. *ChemCatChem*, 11(17):4420-4426, 2019.

[40] Pourzare, K., Farhadi, S., and Mansourpanah, Y. Graphene oxide/Co_3O_4 nanocomposite: synthesis, characterization, and its adsorption capacity for removal of organic dye pollutants from water. *Acta Chimica Slovenica*, 64(4):945-958, 2017.

[41] Lasfargues, M., Bell, A., and Ding, Y. In situ production of titanium dioxide nanoparticles in molten salt phase for thermal energy storage and heat-transfer fluid applications. *Journal of Nanoparticle Research*, 18(6):1-1, 2016.

[42] Zhang, T., He, C., Sun, F., Ding, Y., Wang, M., Peng, L., Wang, J. and Lin, Y. Co_3O_4 nanoparticles anchored on nitrogen-doped reduced graphene oxide as a multifunctional catalyst for H_2O_2 reduction, oxygen reduction and evolution reaction. *Scientific Reports*, 7(1):1-11, 2017.

[43] Diallo, A., Beye, A. C., Doyle, T. B., Park, E., and Maaza, M. Green synthesis of Co_3O_4 nanoparticles via Aspalathus linearis: physical properties. *Green Chemistry Letters and Reviews*, 8(3-4):30-36, 2015.

[44] Reddy, K. P., Jain, R., Ghosalya, M. K., and Gopinath, C. S. Metallic cobalt to spinel Co_3O_4–electronic structure evolution by near-ambient pressure photoelectron spectroscopy. *The Journal of Physical Chemistry C*, 121(39):21472-21481, 2017.

[45] Wang, X., Li, X., Mu, J., Fan, S., Chen, X., Wang, L., Yin, Z., Tade, M. and Liu, S. Oxygen vacancy-rich porous Co_3O_4 nanosheets toward boosted NO reduction by CO and CO oxidation: Insights into the structure–activity relationship and performance enhancement mechanism. *ACS Applied Materials & Interfaces*, 11(45):41988-41999, 2019.

[46] Si, J., Xiao, S., Wang, Y., Zhu, L., Xia, X., Huang, Z., and Gao, Y. Sub-nanometer Co_3O_4 clusters anchored on TiO_2 (B) nano-sheets: Pt replaceable Co-catalysts for H_2 evolution. *Nanoscale*, 10(5):2596-2602, 2018.

[47] Wang, Z., Wang, W., Zhang, L., and Jiang, D. Surface oxygen vacancies on Co_3O_4 mediated catalytic formaldehyde oxidation at room temperature. *Catalysis Science & Technology*, 6(11):3845-3853, 2016.

[48] Fujimoto, A., Yamada, Y., Koinuma, M., and Sato, S. Origins of sp^3C peaks in C1s X-ray photoelectron spectra of carbon materials. *Analytical Chemistry*, 88(12):6110-6114, 2016.

[49] Goswami, C., Yamada, Y., Matus, E. V., Ismagilov, I. Z., Kerzhentsev, M., and Bharali, P. Elucidating the role of oxide–oxide/carbon interfaces of CuO_x–CeO_2/C in boosting electrocatalytic performance. *Langmuir*, 36(49):15141-15152, 2020.

[50] Hu, T., Wang, Y., Zhang, L., Tang, T., Xiao, H., Chen, W., Zhao, M., Jia, J. and Zhu, H. Facile synthesis of PdO-doped Co_3O_4 nanoparticles as an efficient bifunctional oxygen electrocatalyst. *Applied Catalysis B: Environmental*, 243:175-182, 2019.

[51] Wang, Q., Hu, W. H., and Huang, Y. M. One-Pot Synthesis of $Co/Co_3O_4/Co(OH)_2$/N-doped mesoporous carbon for both oxygen reduction reactions and oxygen evolution reactions. *ChemistrySelect*, 2(10):3191-3199, 2017.

[52] Goswami, C., Hazarika, K. K., Yamada, Y., and Bharali, P. Nonprecious hybrid metal oxide for bifunctional oxygen electrodes: Endorsing the role of interfaces in electrocatalytic enhancement. *Energy & Fuels*, 35(16):13370-13381, 2021.

[53] Wang, D., Chen, X., Evans, D. G., and Yang, W. Well-dispersed Co_3O_4/Co_2MnO_4 nanocomposites as a synergistic bifunctional catalyst for oxygen reduction and oxygen evolution reactions. *Nanoscale*, 5(12):5312-5315, 2013.

[54] Alegre, C., Busacca, C., Di Blasi, A., Di Blasi, O., Aricò, A. S., Antonucci, V., Modica, E. and Baglio, V. Electrospun carbon nanofibers loaded with spinel-type cobalt oxide as bifunctional catalysts for enhanced oxygen electrocatalysis. *Journal of Energy Storage*, 23:269-277, 2019.

[55] Alegre, C., Busacca, C., Di Blasi, O., Antonucci, V., Aricò, A. S., Di Blasi, A., and Baglio, V. A combination of CoO and Co nanoparticles supported on electrospun carbon nanofibers as highly stable air electrodes. *Journal of Power Sources*, 364:101-109, 2017.

[56] Han, X., He, G., He, Y., Zhang, J., Zheng, X., Li, L., Zhong, C., Hu, W., Deng, Y. and Ma, T.Y. Engineering catalytic active sites on cobalt oxide surface for enhanced oxygen electrocatalysis. *Advanced Energy Materials*, 8(10):1702222, 2018.

[57] Niu, Y., Huang, X., Zhao, L., Hu, W., and Li, C. M. One-pot synthesis of $Co/CoFe_2O_4$ nanoparticles supported on N-doped graphene for efficient bifunctional oxygen electrocatalysis. *ACS Sustainable Chemistry & Engineering*, 6(3):3556-3564, 2018.

[58] Zhu, Y., Liu, X., Jin, S., Chen, H., Lee, W., Liu, M., and Chen, Y. Anionic defect engineering of transition metal oxides for oxygen reduction and evolution reactions. *Journal of Materials Chemistry A*, 7(11):5875-5897, 2019.

[59] Xu, L., Jiang, Q., Xiao, Z., Li, X., Huo, J., Wang, S., and Dai, L. Plasma-engraved Co_3O_4 nanosheets with oxygen vacancies and high surface area for the oxygen evolution reaction. *Angewandte Chemie International Edition*, 128(17):5363-5367, 2016.

[60] Zhuang, L., Ge, L., Yang, Y., Li, M., Jia, Y., Yao, X., and Zhu, Z. Ultrathin iron-cobalt oxide nanosheets with abundant oxygen vacancies for the oxygen evolution reaction. *Advanced Materials*, 29(17):1606793, 2017.

[61] Liu, Z., Wang, G., Zhu, X., Wang, Y., Zou, Y., Zang, S., and Wang, S. Optimal geometrical configuration of cobalt cations in spinel oxides to promote oxygen evolution reaction. *Angewandte Chemie International Edition*, 59:4736–4742, 2020.

Insight into the Structure-Activity Relationship of Sponge-like Structured Co_3O_4/C Electrocatalyst

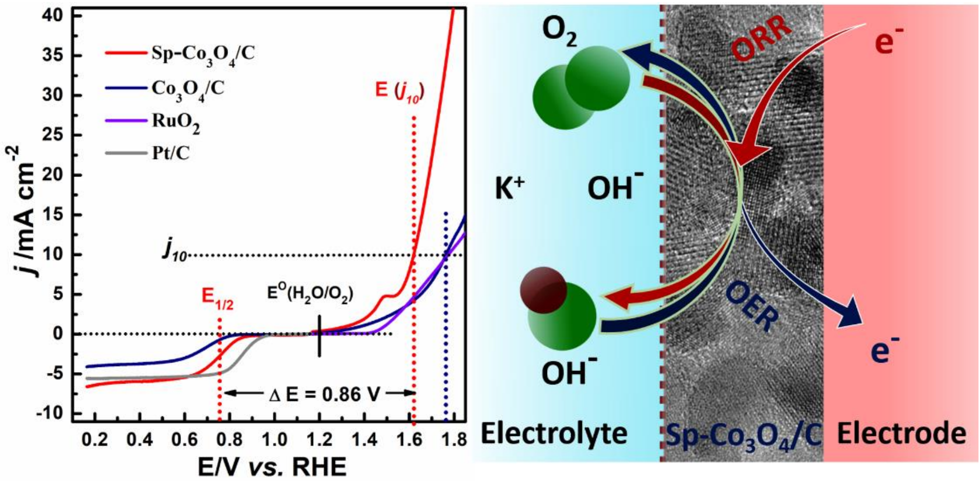

This section of chapter 3 delivers the fabrication of a spongelike morphology Co_3O_4 supported on carbon to investigate the elegant enhachment of its intrinsic properties for bifunctional ORR and OER electrocatalysis. The significant structural properties of Sp-Co_3O_4/C, such as exposed facets, surface atomic configurations, the higher specific surface area, the higher ECSA, surface oxygen vacancies along with the electronic effects of Co^{2+} and Co^{3+} around the oxide-oxide interfacial area have been highlighted. In combination with the analysed structural properties of Sp-Co_3O_4/C, the electrocatalytic performance have been tested for bifunctional ORR and OER to established the structure-activity relationship. We have used a facile two step solvothermal route to fabricate the EC. The detail experimental procedure for the synthesis, physicochemical and electrochemical characterization used in this section were discussed in Chapter 2.

3B.1. Introduction

The critical issues posed by the depletion of fossil fuels and changing the global climate have compelled the scientific community to seek out environmentally beneficial, long-term, and efficient energy sources [1-3]. As a sustainable energy carrier, hydrogen is one of the most potential fossil fuel substitutes because it doesn't produce carbon emissions [4-5]. FCs and MABs are the most promising energy conversion and storage devices that directly generate electricity from chemical energy of hydrogen. The PEMFC and unitized regenerative PEMFC have been studied for decades among all forms of fuel cells. However, the efficiency of both PEMFC and URPEMFC is critically restrained by the slow kinetics of the ORR on the cathode and OER on the anode [6-10]. The design of the efficient bifunctional ORR/OER ECs can boost both the discharge and charge mechanism of URPEMFC and MABs. Hence, a high-performance bifunctional EC is required to diminish the ORR/OER overpotential as the usual kinetics of the oxygen reaction is significantly slower. Noble metal-centred ECs, such as Pt, Pd, and Ru are still the state-of-the-art ECs for ORR/OER today, but they account for the major fraction of the entire cost of an FC, limiting its commercialization [11-18].

TMOs have recently attracted enormous attention as prospective cathodic materials because of their low price and high catalytic activity [19-22]. However, these materials have several drawbacks, such as low electrical conductivity and poor electron transfer rate, which have hampered their use in real-world devices. So far, several ways have been used to address these shortcomings, which include combining TMOs with conductive carbon-based support materials. Carbon materials are widely known for their excellent electronic conductivity, high specific surface area, and porous structure, which could make them an appealing host for TMOs [23,24]. To further enrich the active sites along with the intrinsic activities of metal-based ECs, different development strategies have been reported to date [25]. Tailoring the structure of MOs to achieve definite morphologies with substantial oxide-oxide interface and oxygen vacancies has become a significant strategy for the advancement of TMO-based ECs. It is well-established from the crystallographic correlations that the pattern of the atoms on the catalyst's surface is dependent on the shape and size of NPs. However, the correlation between morphology and electrocatalysis has not been well explored or understood yet. Defects and interfaces in nanomaterials are typically distinguished as the active sites for ORR/OER catalytic process owing to the exceptional electronic and surface properties in the local vicinity [26,27]. Cobalt-oxides have been considerably inspected over the past decades for ORR and OER processes because of the low cost of Co and its easy accessibility. Various chemical compositions, crystalline structures, and multi-valence of Co state in Co-oxides trigger them as a class of promising bifunctional ORR/OER ECs in alkaline electrolytes [28-31]. Recently, the electrocatalytic functioning of nanocactus-like Co_3O_4/CNTs structure [28], Co_3O_4 nanosheet-graphene composite (Co-S/G-3) [29], N-doped reduced graphene oxide supported $CuCo_2O_4$ [30], and covalent hybrid of spinel $MnCo_2O_4$/N-rmGO [31] have been reported as efficient ORR/OER EC, which are dependent on morphology-controlled surface facets and the surface active sites.

To tailor the active sites in Co-oxide for ORR/OER electrocatalysis, herein we report a morphology-controlled synthesis of surface-modified Co_3O_4 NPs via a facile two-step solvothermal approach. We demonstrate that polycrystalline Co_3O_4 NPs supported on carbon, which exhibit a sub-standard bifunctional ORR/OER performance, but when designed with a sponge-like (Sp) hollow structure with a high surface area and rich oxide-oxide interface structure that is anchored on carbon (Sp-Co_3O_4/C) unveils astonishingly enhanced bifunctional performance for ORR/OER in alkaline electrolyte. The morphology-controlled Sp-Co_3O_4/C demonstrates superior stability and ORR current densities, comparable to the ORR performance exhibited by commercial Pt/C EC (20 Wt.%). Similarly, its OER performance was observed to be better than standard RuO_2 in identical experimental conditions. The excellent electrocatalytic ORR/OER bifunctionality is directed by the exposed oxygen-deficient interfacial structures of (111), (220), and (311) crystal facets, in the hollow sponge-like Co_3O_4 morphology, pointing to the Co^{2+} and Co^{3+} ions as the ORR and OER active sites, respectively.

3B.2. Results and Discussion

3B.2.1. Structural and Morphological Characterization

The synthesis of Co_3O_4 with sponge-like morphology is systematically portrayed in Scheme 2.2.2 of chapter 2. Briefly, the preparation process comprises a facile two-step solvothermal reaction in a 1:1 v/v ethylene glycol/deionized water system followed by sintering. The XRD patterns presented in Figure 3B.1 show the diffraction peaks for the investigated samples that could be indexed to both the Sp-Co_3O_4/C and Co_3O_4/C phases. Sp-Co_3O_4/C exhibited higher peak intensity compared to that of Co_3O_4/C because of its higher crystalline nature. The diffractions spotted at angles (2θ) 19.1°, 31.3°, 36.9°, 38.6°, 44.9°, 55.8°, 59.5° and 65.4° belong to the Co_3O_4 cubic phase in both Sp-Co_3O_4/C and Co_3O_4/C with a lattice constant of

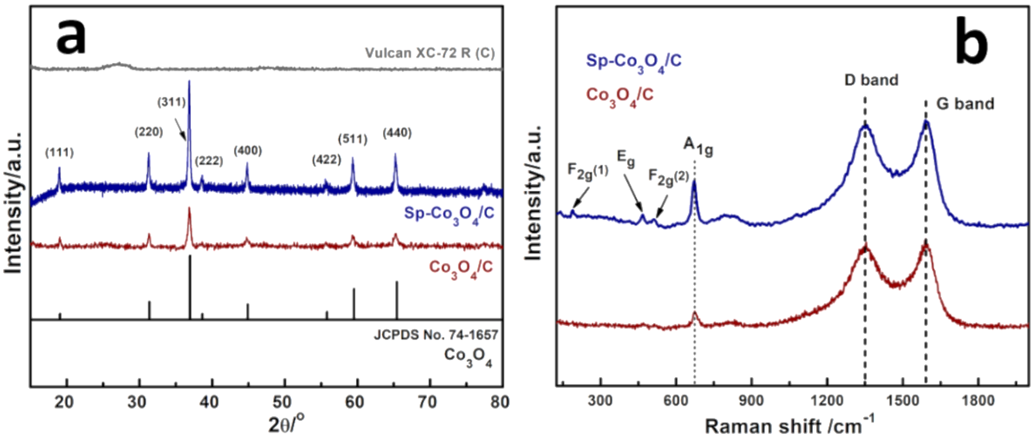

Figure 3B.1. (a) XRD patterns of C, Sp-Co_3O_4/C, and Co_3O_4/C and b) Raman spectra of Sp-Co_3O_4/C and Co_3O_4/C.

a = 8.065 Å and a space group of Fd3m, which are in agreement with the JCPDS no. 74-1657 [32]. The XRD peak (2θ=24°) related to the graphitic C-sp^2 structure of carbon in Sp-Co_3O_4/C and Co_3O_4/C has not appeared, indicating poor crystallinity [33]. Two characteristic Raman peaks at 1365 and 1595 cm^{-1} are found in Sp-Co_3O_4/C and Co_3O_4/C (Figure 3B.1 b). The peak at 1365 cm^{-1} is signified as the D band spectrum and it is characteristic of defects, while the peak at 1595 cm^{-1} belongs to the G band that appears due to the E_{2g} mode of sp^2-bonded carbon atoms [34,35]. The Raman spectrum of the Sp-Co_3O_4/C in the range of 400–800 $cm^{–1}$ shows four obvious peaks located at around ~189.6, ~467.5, ~513.2, and ~672.3 $cm^{–1}$, corresponding to Co_3O_4. The Raman peaks for Co_3O_4/C seem to be lower in intensity relative to that of Sp-Co_3O_4/C because of the poor crystallinity of Co_3O_4/C. The strong band at about 675 $cm^{–1}$ is ascribed to the octahedral sites (O_h-$Co^{III}O_6$) of Co_3O_4 (A_{1g} symmetry), whereas the F_{2g} and E_g modes are endorsed to the collective vibrations of the O_h and tetrahedral site (T_d) oxygen motions [36,37]. However, the peak positions of A_{1g} and F_{2g}(1) were shifted to lower wavenumbers about 18.7 and 4.8 $cm^{–1}$, respectively, compared with bulk Co_3O_4. This spectacle is ascribed to the crystal size-induced effect of optical phonon confinement in NPs, creating uncertainty in the phonon wave vectors and followed by Raman peaks' downshift. The downshift of the A_{1g} and F_{2g}(1) mode can be further correlated to the exposure of more surface oxygen vacancies, which is significant for the stimulation of oxygen electrocatalysis [38-40].

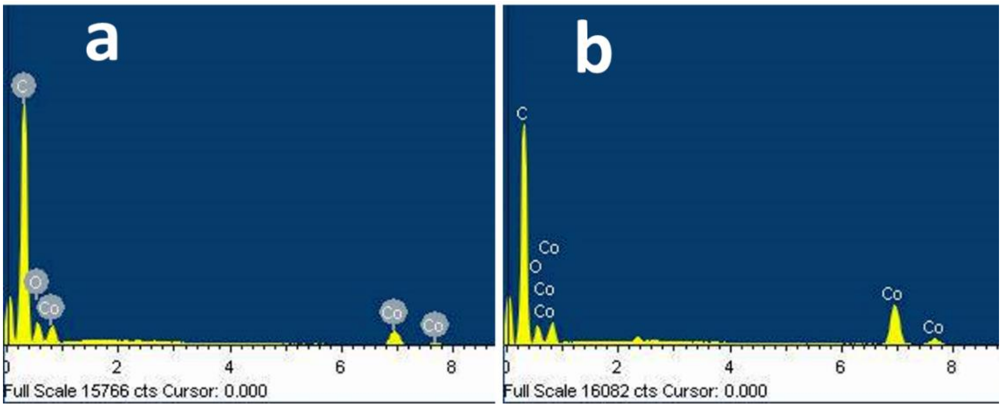

Figure 3B.2. EDX spectra of the ECs. a) Co_3O_4/C and b) Sp-Co_3O_4/C.

The element and atomic percentages (At.%) of Co_3O_4/C and Sp-Co_3O_4/C were performed by EDX analysis. The At.% of Co, O and C in Sp-Co_3O_4/C were 3.90, 12.58 and 83.52 %, respectively. The EDX spectra along with the quantitative elemental compositions in both Sp-Co_3O_4/C and Co_3O_4/C materials are summarized in Figure 3B.2 and Table 3B.1.

Table 3B.1. Physical properties of the as-prepared ECs.

Electrocatalysts (ECs)	Element	Wt.% [a]	At.% [a]	BET surface area (m^2/g)	Av. Pore size (nm)
Co_3O_4/C	C	71.74	80.59	123	3.2
	O	21.06	17.76		
	Co	7.20	1.65		
Sp-Co_3O_4/C	C	69.94	83.52	131.5	3.5
	O	14.03	12.58		
	Co	16.03	3.90		

[a] The Wt.% and At.% are evaluated based on EDX measurement.

The morphology of Sp-Co_3O_4 nanostructures was investigated by SEM imaging technique (Figure 3B.3a-c). The SEM images of Sp-Co_3O_4 demonstrated the sponge-like morphology within the dimension of below 3 μm that appreciably aggregated as clusters of extraordinarily small dimensions and high surface energy of the attained NPs. The SEM image reveals asymmetrical particle agglomerates of the NPs, signifying that the prepared Sp-Co_3O_4 is constituted of plentiful NPs undergoing further accumulation to form a porous agglomerate structure. The average particle size distribution of Sp-Co_3O_4 was evaluated from the TEM image which was observed to be ~ 5.5 nm (inset of Figure 3B.3 g). We further investigated the crystallographic texture of the Sp-Co_3O_4 using the HRTEM technique. The HRTEM images as shown in Figure 3B.3 d demonstrate the sponge-like texture whereas Figure 3B.3 e shows the

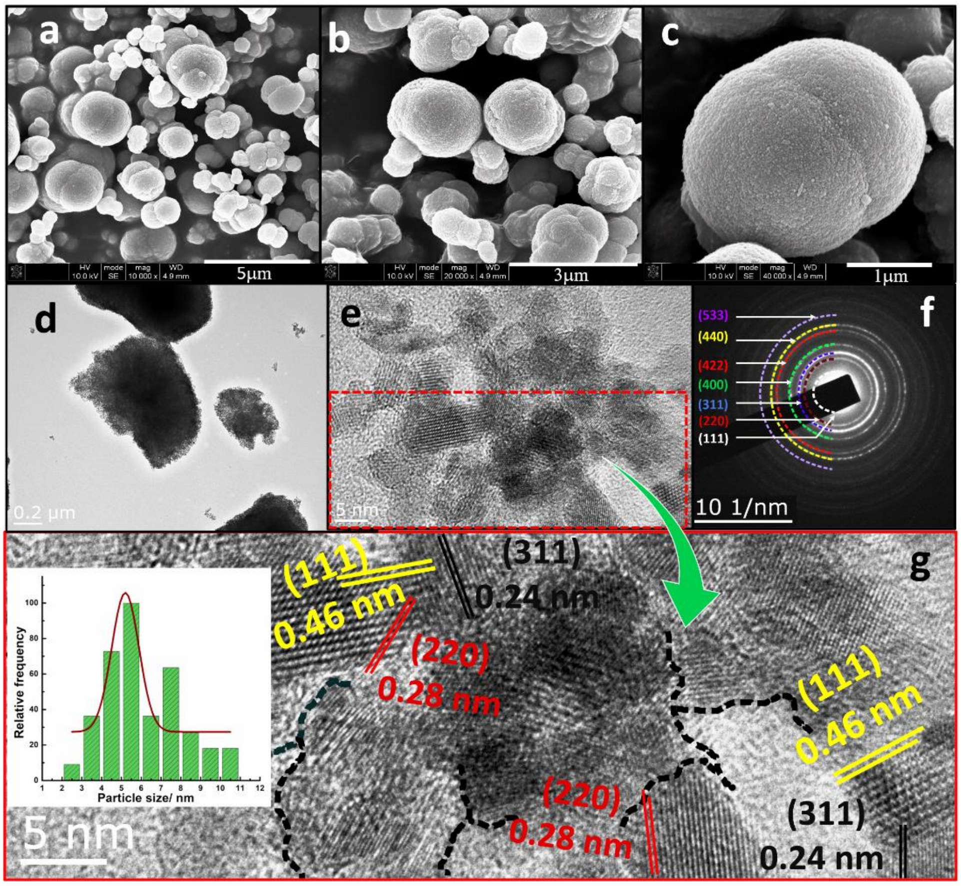

Figure 3B.3. (a-c) SEM images, d, e) HRTEM images, f) SAED pattern of Sp-Co_3O_4/C, and g) magnified display of the HRTEM image in the area under the red rectangle in (e) and the inset of (g) represents the particle size distribution obtained from the HRTEM image (e).

well-ordered and regular dissemination of NPs with abundant facets. The SAED pattern (Figure 3B.3 f) exposes the various crystal facets of Sp-Co_3O_4, which are consistent with the XRD diffraction planes. Figure 3B.3 g presents the magnified view of the area under the red rectangle of Figure 3B.3 e. The d-spacing of lattice fringes were estimated to be 0.46, 0.28 and 0.24 nm, corresponding to (111), (220) and (311) crystal planes, respectively that are consistent with the SAED and XRD pattern of Sp-Co_3O_4. The distinct and different exposed facets, predominantly (111), (220) and (311) are appeared to be distributed in random orientations, building various oxide-oxide interfaces. Interfaces in heterogeneous catalysts are sort of areas in between adjacent moieties, which possess unavoidable defects, providing unique characteristics relative to their parent materials. The defects in the interfaces expose the sites for the effective electrocatalytic process for ORR and OER. The microscopic images of the Co_3O_4 synthesized by hydrothermal synthesis at 180 °C are shown in Figure 3B.4. These images reveal the polycrystalline nature of Co_3O_4 in the microscopic dimensions.

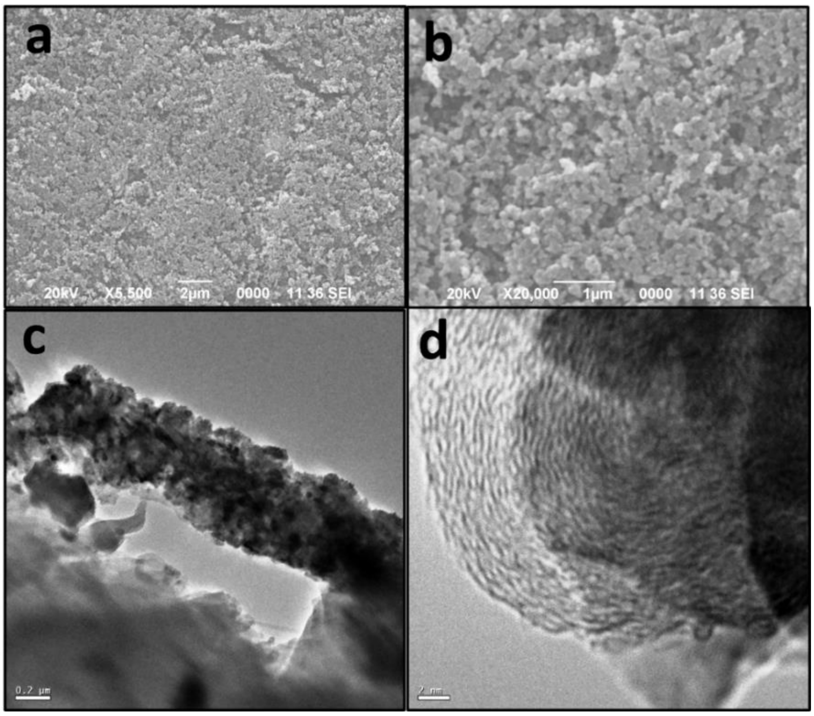

Figure 3B.4. a, b) SEM images of Co_3O_4 and c, d) TEM and HRTEM images of Co_3O_4.

The Co_3O_4 Wt.% in Sp-Co_3O_4/C and Co_3O_4/C were assessed using TGA analysis. Figure 3B.5 a presents the TGA curves showing the sequential degradation of carbon components with an increase in temperature. Eventually, the weight loss became stable at ~ 500 °C with a loss of ∼70 Wt.%, which is because of the decay of carbon at higher temperatures suggesting residual ∼30 Wt.% is the Co_3O_4 content in the material. The specific surface area and mesoporous texture of the Sp-Co_3O_4/C and Co_3O_4/C were characterized by N_2 adsorption-desorption isotherms at the liquid N_2 temperature, as shown in Figures 3B.5 b and c. The isotherms for both Sp-Co_3O_4/C and Co_3O_4/C corresponded to characteristic type IV with an H3-type hysteresis loop, signifying the slit-like shaped pores [41]. The calculated specific surface areas for Sp-Co_3O_4/C and Co_3O_4/C are 131.5 and 123 m^2g^{-1} respectively. As shown in the inset of Figures 3B.5 c and d, the pore size distribution curves displayed a narrow peak at around 3-4 nm suggesting the porous nature of the materials. The average pore diameters were obtained to be 3.5 and 3.2 nm, respectively, for Sp-Co_3O_4/C and Co_3O_4/C.

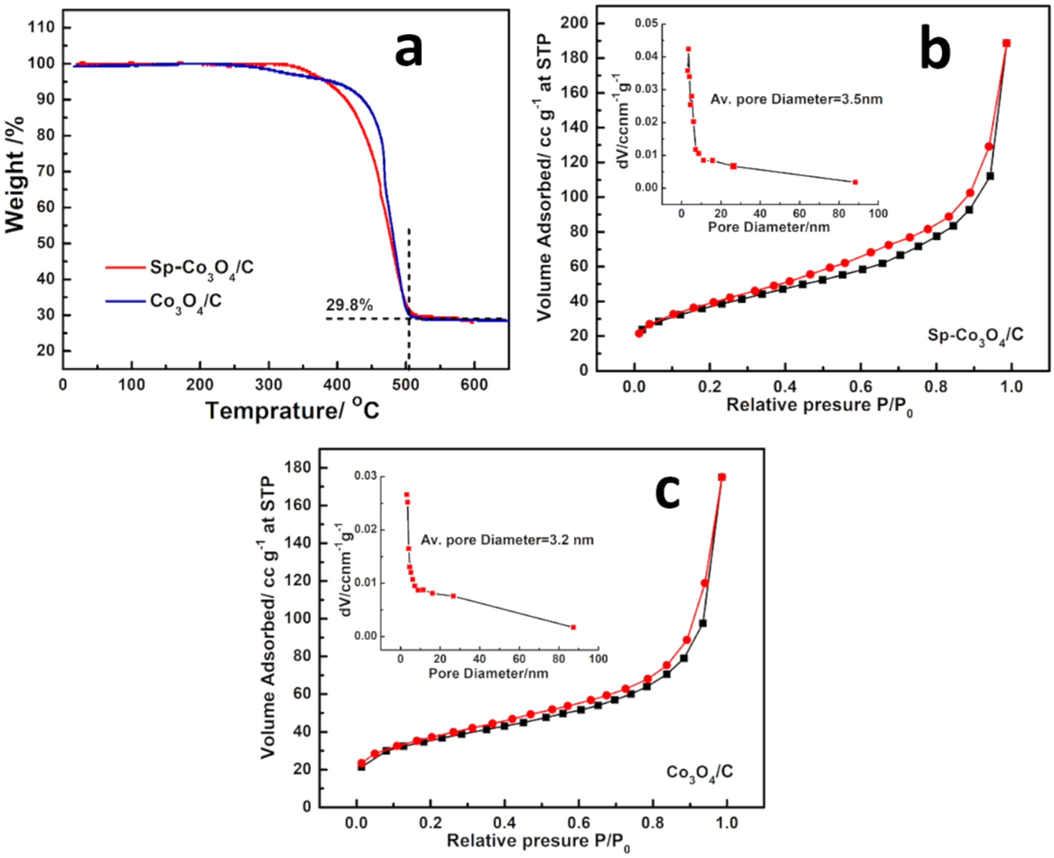

Figure 3B.5. a) TGA profile of Sp-Co_3O_4/C and Co_3O_4/C, b, c) N_2 adsorption-desorption isotherms of Sp-Co_3O_4/C and Co_3O_4/C respectively (plots in the insets are the pore size distribution curves for the respective ECs).

XPS analysis is used to study the surface compositions and oxidation states of Co in Sp-Co_3O_4/C. Figure 3B.6 (a-d) shows the XPS spectrum of Co 2p, C 1s and O 1s along with the survey spectrum of Sp-Co_3O_4/C, which are standardized by calibration with C 1s peak (284.4 eV) before analyzing the binding energies (BE). The survey spectrum (Figure 3B.6 a) displays the relative peak intensity and position in BE of the exclusive elements in Sp-Co_3O_4/C viz. C, O and Co indicate the high purity of the sample material. Figure 3B.6 b shows the deconvolution peaks of C 1s exposing the C state in Sp-Co_3O_4/C. The distinct peaks at 284.4 and 285.4 eV could be attributed to the –C=C–, –C–O– groups, respectively, while the weak peak at ~288.6 eV could be assigned to the O=C–O group. The resultant peak area produced by the peak for –C=C– and O=C–O group implies the population density of sp^2-C, which is significant for the electrical conductance of the synthesized materials.

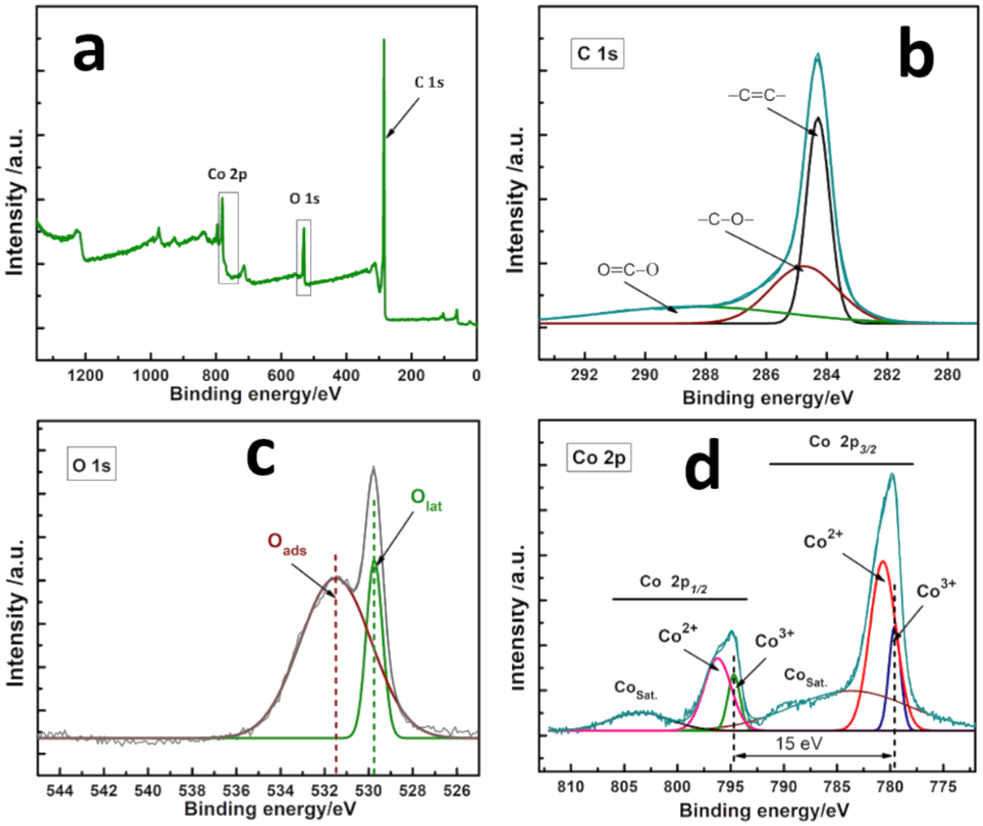

Figure 3B.6. XPS survey spectrum of Sp-Co_3O_4/C (a), core-level XPS spectrum of C 1s (b), O 1s (c) and Co 2p (d).

Similarly, the deconvoluted O 1s spectrum shows two distinct peaks at 529.7 and 531.5 eV (Figure 3B.6 c) signifying the lattice oxygen (O_{lat}) and the adsorbed oxygen

(O_{ads}) on the surface of Sp-Co_3O_4/C, respectively [42]. The O_{lat} state is characteristic of metal-oxygen bonding interaction in the lattice. Figure 3B.6 d shows the Co 2p XPS spectrum, comprising a doublet positioned at ~781.2 (Co $2p_{3/2}$) and ~796.2 eV (Co $2p_{1/2}$) with 15 eV spin-orbit splitting, along with two characteristics satellite peaks at ~783.2 and ~803.7 eV [43]. The Co $2p_{3/2}$ and Co $2p_{1/2}$ are further split into two components that could be assigned to Co^{3+} and Co^{2+} states, where Co^{3+} acquires lower BE as reported by previous studies [44-46]. Hence, the peaks with the BE of 781.2 and 796.2 eV are ascribed to Co^{3+} which is confined in O_h oxygen coordination whereas the peak at 794.5 and 779.6 eV are ascribed to Co^{2+} with T_d coordination of the spinel Sp-Co_3O_4. The surface oxygen vacancy of Sp-Co_3O_4/C can be qualitatively measured from the Co^{2+}/Co^{3+} ratio, which specifies the availability of defective sites as well. The Co^{2+}/Co^{3+} ratio for Sp-Co_3O_4 is evaluated to be 3.2, suggesting the accumulation of a rich oxygen vacancy in the EC.

3B.2.2. Electrocatalytic Activity

To evaluate the ORR and OER performance of the ECs, a series of electrochemical tests are accomplished. The primary analysis to assess the ORR activity of the synthesized ECs was conducted by the CV method. Figure 3B.7 a shows the CV curves obtained for carbon (C), Sp-Co_3O_4/C, and Co_3O_4/C in both N_2- and O_2-saturated 0.1 M KOH solutions. The CV curves in dotted lines represent the electrochemical activity in the N_2-saturated atmosphere, whereas the solid lines of the corresponding indicate the ORR performance, with significant reduction peaks, suggesting the ORR active nature of the ECs. Sp-Co_3O_4/C demonstrates a superior ORR onset potential (E_{onset}) of 0.88 V (vs. RHE) in comparison to that exhibited by C (0.77 V) and Co_3O_4/C (0.79 V).

For a more comprehensive ORR study, linear sweep voltammetry (LSV) test with RDE was conducted in an O_2-saturated 0.1 M KOH electrolyte. Figure 3B.7 b and c show the LSV polarization curves obtained for Co_3O_4/C and Sp-Co_3O_4/C recorded at various rotations. As expected, the E_{onset} values obtained from the LSV curves are consistent with the CV study. A comparative analysis of limiting current density (*j*) for C, Pt/C, Sp-Co_3O_4/C, and Co_3O_4/C recorded at 1600 rpm is presented in Figure 3B.7 d. Sp-Co_3O_4/C demonstrates a superior *j* value of – 6.60 mA cm^{-2} compared to that of C (–1.9 mA cm^{-2}) and Co_3O_4/C (–4.09 mA cm^{-2}) and commercial Pt/C (–5.50 mA cm^{-}

^{2}). The half-wave potential ($E_{1/2}$) is observed to be 0.60, 0.84, 0.67 and 0.75 V, respectively for C, Pt/C, Co_3O_4/C, and Sp-Co_3O_4/C.

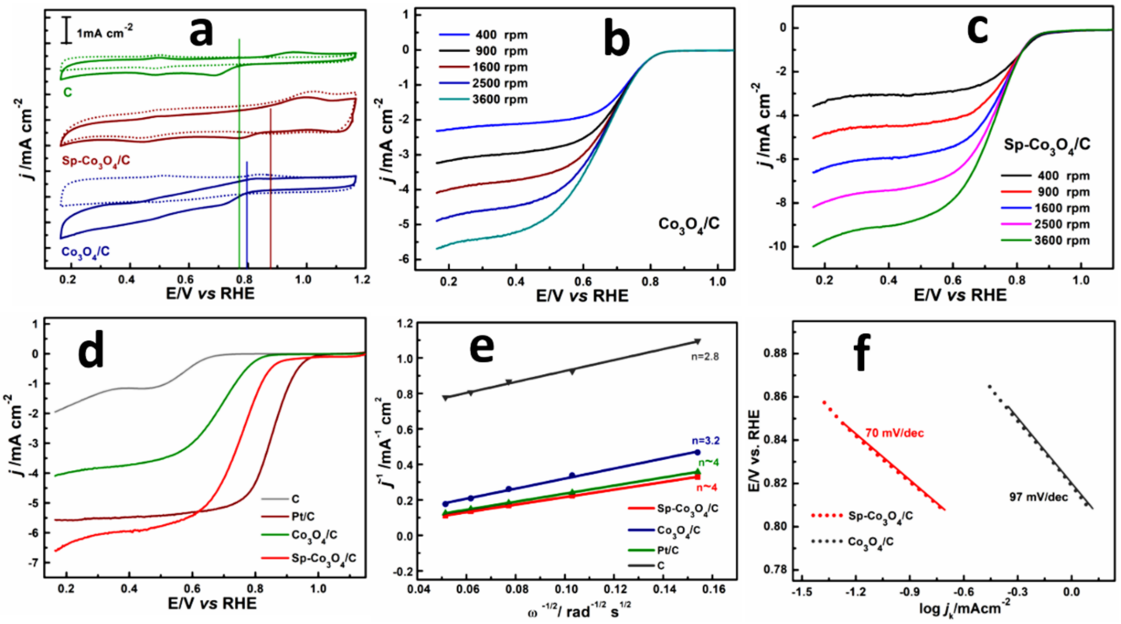

Figure 3B.7. a) CVs of C, Sp-Co_3O_4/C, and Co_3O_4/C in N_2 (dotted lines) and O_2 (solid lines) saturated 0.1 M KOH solution, b) ORR LSV curves of Co_3O_4/C, c) ORR LSV curves of Sp-Co_3O_4/C, d) LSV curves of C, Pt/C, Sp-Co_3O_4/C, and Co_3O_4/C at 1600 rpm, e) K-L plot at 0.50 V, f) Tafel plots of Sp-Co_3O_4/C and Co_3O_4/C.

The ‘n’ value is calculated from the B factor of the Koutecky−Levich (K−L) equation [47]. Figure 3B.7 e displays the K-L plots obtained for the ECs at 0.40 V. It is observed that both Sp-Co_3O_4/C and Pt/C favour the ORR in the direct $4e^-$ pathway without developing any intermediate product. On the contrary, both Co_3O_4/C and C facilitate an indirect ORR pathway with ‘n’ values of 3.2 and 2.8, respectively. The K−L plots’ linearity and the near parallelism of the fitting lines are observed to be coherent with the first-order reaction kinetics. Additionally, it suggests a similar number of electron transfers for the ORR process. The kinetics of the ORR process on the ECs surface is investigated with the Tafel slope in the kinetically controlled region of the LSV polarization curve at 1600 rpm. Sp-Co_3O_4/C displays a lower Tafel slope of 70 mV dec^{-1} indicating faster ORR kinetics in contrast to that of Co_3O_4/C (97 mV dec^{-1}) as presented in Figure 3B.7 f.

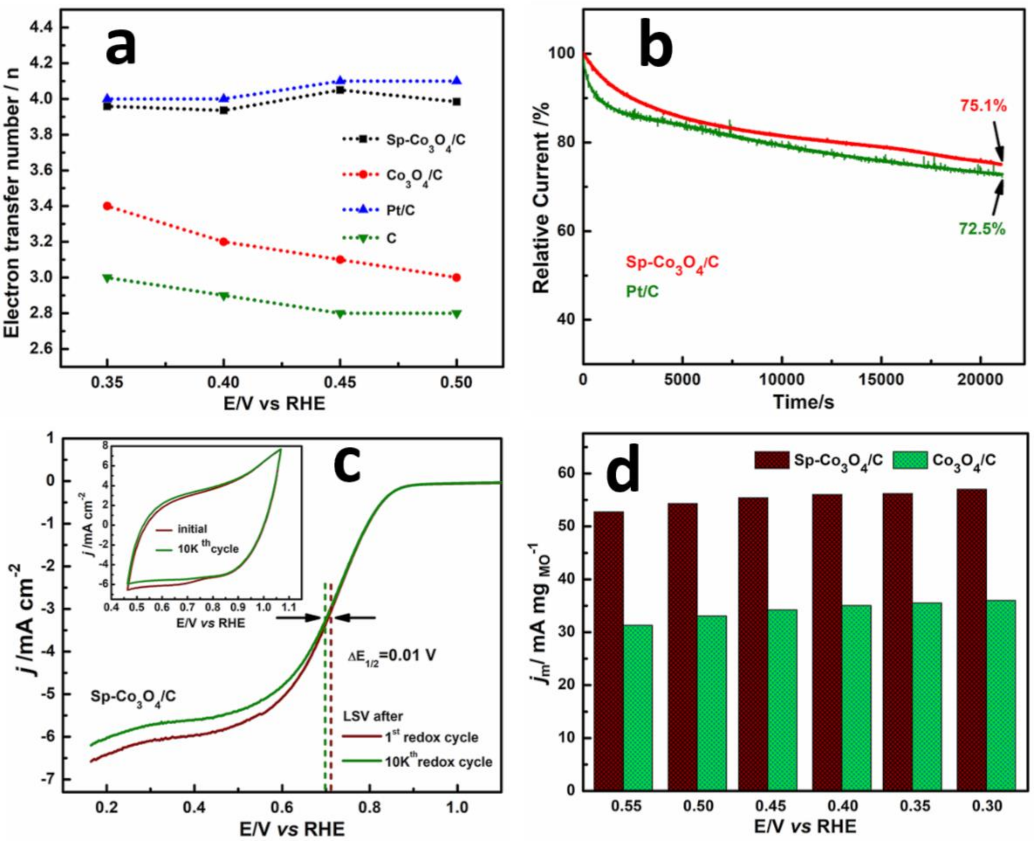

Figure 3B.8. a) Plot of electrons transfer number at a wide potential range, b) chronoamperometric (CA) test, c) accelerated durability test (ADT), and d) mass-specific activity (MA) at 1600 rpm.

A consistent 4e$^-$ ORR process over a wide potential range is crucial for an effective EC. Figure 3B.8 a represents the plot of ‘n’ values obtained for different potentials which reveals that Sp-Co_3O_4/C follows a consistent 4e$^-$ route over a wide potential range that is comparable to the activity possessed by Pt/C. The CA test as shown in Figure 3B.8 b establishes the better stability of the EC Sp-Co_3O_4/C. It is observed that Sp-Co_3O_4/C shows higher retention of its initial current (75.1%), while Pt/C shows 72.5% of current in the CA operation recorded up to 6 h. The durability of Sp-Co_3O_4/C is further analyzed with the accelerated durability test. The comparison of the initial and the final ORR polarization curves after the operation of 10000 redox cycles is shown in Figure 3B.8 c. The observed $\Delta E_{1/2}$ (0.01 V) is significantly slighter after the 10000 redox cycle, suggesting the significantly higher durability unveiled by the catalyst Sp-Co_3O_4/C.The mass activity for the inspected ECs in the potential range of 0.30-0.55 V is evaluated and shown in Figure 3B.8 d. Sp-Co_3O_4/C reveals higher mass activity (~ 52-58 mA mg $_{MO}^{-1}$ at all investigated potential) compared to that of Co_3O_4/C which portrays the characteristic higher intrinsic ORR activity of the sponge-like EC.

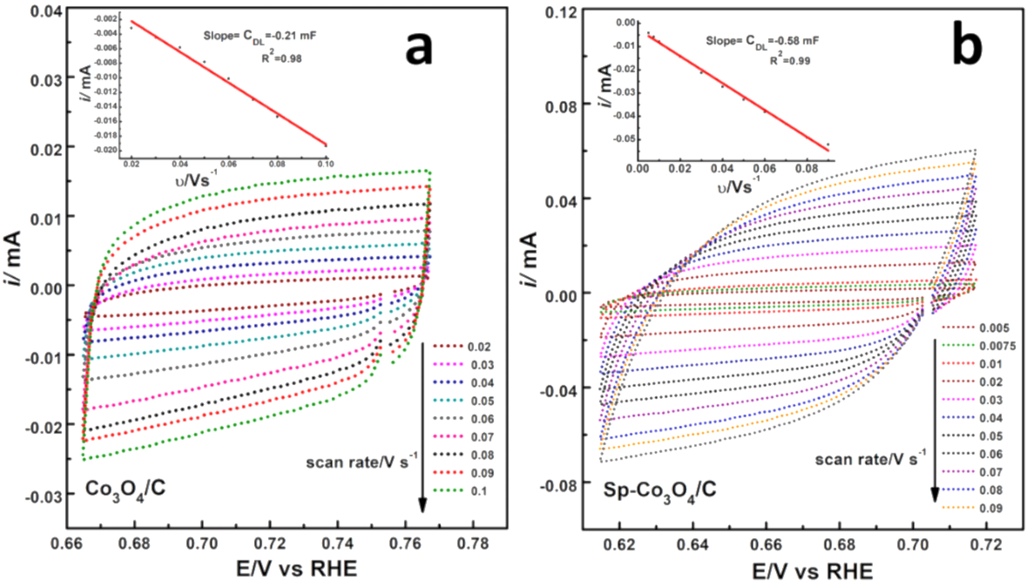

Figure 3B.9. C_{dl} measurements for determining ECSA in 0.1 M KOH. a, b) CVs of Co_3O_4/C and Sp-Co_3O_4/C at various scan rates (Corresponding insets represent the slope of scan rate vs. current obtained from the respective CV data).

The ECSA is an important parameter that influences the electrochemical activities of ECs. The details of the double-layer capacitance (C_{dl}) method used to estimate the ECSA of the ECs are discussed in the previous section. The C_{dl} of Co_3O_4/C and Sp-Co_3O_4/C are evaluated using CV at various scan rates (Figures 3B.9a and b. Sp-Co_3O_4/C possesses an ECSA of 48.33 m^2 g^{-1}, which is much higher than the ECSA of Co_3O_4/C (17.50 m^2 g^{-1}). This study reveals that Sp-Co_3O_4/C exposes more active sites for oxygen electrocatalysis facilitating the enhanced activity. The higher ECSA of the Sp-Co_3O_4/C can be attributed to the characteristic synergy within the sponge-like Co_3O_4 morphology and the carbon support. The number of electrons (n) that transfers in an elementary ORR is significant as the energy converting and storage devices demand a 4e$^-$ ORR process.

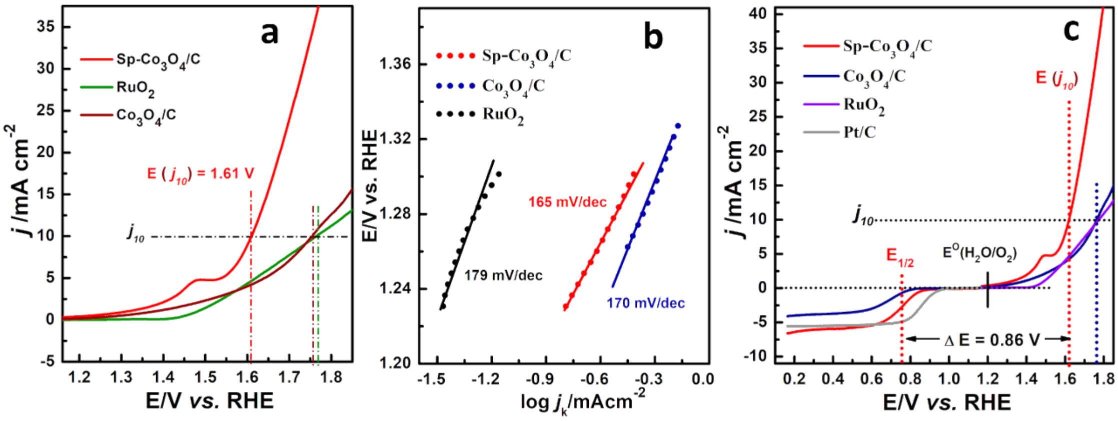

Figure 3B.10. a) OER activity of Sp-Co_3O_4/C compared with RuO_2 and Co_3O_4/C, b) OER Tafel plots for Sp-Co_3O_4/C, Co_3O_4/C, and RuO_2, c) bifunctional ORR/OER performance of Sp-Co_3O_4/C and Co_3O_4/C.

The OER activity of ECs is investigated with the LSV technique in 0.1 M N_2-saturated KOH solution. Figure 3B.10 a shows the OER performance of Sp-Co_3O_4/C and Co_3O_4/C, which is compared with the OER activity of the benchmark RuO_2. Sp-Co_3O_4/C displayed superior OER activity with an E_{onset} of 1.24 V to that of Co_3O_4/C (E_{onset}= 1.26 V) and RuO_2 (E_{onset}= 1.43 V). The current density of 10 mA cm^{-2} (j_{10}) for OER is considered as a baseline factor to assess the OER efficiency of ECs [48]. The OER study from the LSV curves reveals that Sp-Co_3O_4/C attains a 10 mA cm^{-2} current density at an overpotential (η_{10}) of 0.38 V, while the η_{10} values for Co_3O_4/C and RuO_2 are observed to be 0.52 and 0.53 V respectively, suggesting the superior OER activity Sp-Co_3O_4/C.

The reversibility index is a useful parameter to evaluate the associative bifunctional nature, which is calculated by the variance of OER and ORR metrics ($\Delta E = E_{j10} - E_{1/2}$) [48,55]. The reversibility is more feasible when an EC possess a lesser ΔE. Hence, a high-performance bifunctional EC should perform the electrocatalytic activity with a low value of ΔE. The bifunctional ORR/OER performance of Sp-Co_3O_4/C and Co_3O_4/C is shown in Figure 3B.10 c. Sp-Co_3O_4/C exhibited a significantly smaller ΔE value (0.86 V) than that of Co_3O_4/C (1.08), which is comparable to the noble-metal benchmarks Pt/C and RuO_2 [51] and previously reported bifunctional ECs Co-NC 750 (ΔE = 1.02 V) [50], Co_3O_4-CeO_2/C (ΔE = 1.04

V) [41], Co_3O_4/2.7Co_2MnO_4 (ΔE = 1.09 V) [54] signifying the superior bifunctional performance of Sp-Co_3O_4/C for ORR and OER.

Table 3B.2. Bifunctional ORR/OER activities of recently reported Co- and Co_xO_y-based ECs in 0.1 M KOH medium*

ECs	**ORR**			**OER**		**ΔE = [E(j_{10}) –$E_{1/2}$)] (V)**	**Ref.**
	E_{onset} (V)	$E_{1/2}$ (V)	j (mA cm^{-2})	E(j_{10}) (V)	E_{onset} (V)		
Co_3O_4-CeO_2/C	0.84	0.69	–4.20	1.73	1.20	1.04	[41]
Co_3O_4/NPC	0.83	0.74	~ –4.50	1.63	1.55	0.89	[49]
Co-NC 750	0.87	0.78	~ –5.40	1.80	1.58	1.02	[50]
Co-N/G-600	0.86	0.76	~ –5.20	1.72	1.56	0.96	[51]
Co_3O_4-NC/N-rGO	0.82	0.68	–4.98	1.67	~ 1.62	0.99	[52]
Co_3O_4-NTO/N-rGO	0.84	0.71	–4.95	1.64	~ 1.61	0.93	[52]
Co/$CoFe_2O_4$	0.77	0.63	~ –4.40	1.62	--	0.99	[53]
Co_3O_4/2.7Co_2MnO_4	--	0.68	--	1.77	--	1.09	[54]
Co_3O_4/C	0.79	0.67	–4.09	1.76	1.26	1.08	This work
Sp-Co_3O_4/C	0.88	0.75	–6.60	1.61	1.24	0.86	This work

* The potentials in a Ag/AgCl and SCE electrode were converted vs. RHE: $E_{RHE} = E_{Ag/AgCl} + E^o_{Ag/AgCl} + 0.059$ pH and $E_{RHE} = E_{SCE} + E^o_{SCE} + 0.059$ pH; where, E_{RHE} is the reversible hydrogen electrode potential, $E_{Ag/AgCl}$ is Ag/AgCl electrode potential and $E^o_{Ag/AgCl}$ is standard Ag/AgCl electrode potential = 0.1976 Vat 25 °C while E_{SCE} is calomel electrode potential and $E^o_{Ag/AgCl}$ is standard calomel electrode potential = 0.244 V at 25 °C and pH of 0.1 M KOH = 13

The OER kinetics of the ECs is studied with OER Tafel plots. Figure 3B.10 b portrays that the Sp-Co_3O_4/C displays the lowest Tafel slope of 165 mV dec^{-1} in the lower overpotential region than that of Co_3O_4/C (170 mV dec^{-1}) and RuO_2 (179 mV dec^{-1}), suggesting that Sp-Co_3O_4/C catalyzes with faster oxygen evolution rate at the electrode surface. A comprehensive assessment with various Co- and Co_xO_y-based ECs have presented in Table 3B.2. These outcomes suggest that Sp-Co_3O_4/C is a promising cost-effective and competent bifunctional EC for both ORR and OER. The authenticated mechanism of ORR/OER with the Sp-Co_3O_4/C lingers not profound clear. As revealed in the SEM images (Figure 3B.3 a-c), the Sp-Co_3O_4 possessed a typical sponge-like structure, which could expose more catalytic active sites and offer more spaces for O_2 adsorption and desorption. The high specific surface area (Figure 3a) as well as the higher ECSA of Sp-Co_3O_4/C are the key factors for the enhanced electrocatalytic activity. It is noteworthy that, Co_3O_4 possesses a normal-spinel configuration of $Co^{2+}Co_2^{3+}O_4$, where the Co^{2+} ion in the formula unit inhabits the T_d site and the two Co^{3+} ions reside in the O_h sites [36,37]. The Raman spectrum of Sp-Co_3O_4/C as shown in Figure 3B.3 b illustrates the occupation of the Co^{2+} and Co^{3+} in the T_d and O_h sites, respectively. Similarly, the HRTEM image as shown in Figure 3B.3 g portrays the closely packed exposed facets of (111), (220) and (311) and their surface atomic configurations of the spinel Sp-Co_3O_4 crystals. The carbon-supported Sp-Co_3O_4 could furnish an intensive coupling with the predominantly exposed (111), (220), and (311) crystal facets of the spinal structure, where the electronic effects of Co^{2+} and Co^{3+}, around the oxide-oxide interfacial region play a role in the ORR/OER processes. The active reaction sites in Sp-Co_3O_4/C could be the exposed Co^{2+}/Co^{3+} oxide species at the interface with carbon. Furthermore, the surface oxygen vacancies in the Sp-Co_3O_4/C could promote the activation of adsorbed O_2 by means of the characteristic redox property of the Co^{3+}/Co^{2+} couple [56,57]. Moreover, the surface oxygen vacancies could facilitate an O_2 buffer that elevates the O_2 mobility with enhanced O_2 adsorption/desorption. The coordinated Co^{2+} in Sp-Co_3O_4/C favourably function as the active sites for the ORR, while Co^{3+} triggers the OER process accelerating the overall bifunctional activity [58,59]. Hence, the excellent bifunctional ORR/OER performance of the Sp-Co_3O_4/C can be illustrated by the morphology-dependent structure-activity relationship.

3B.3. Conclusions

In summary, sponge-like microaggregates of Co_3O_4 anchored on carbon support (Sp-Co_3O_4/C) are successfully fabricated via a facile two-step solvothermal route, which performs excellent bifunctional ORR/OER activity in an alkaline medium. Sp-Co_3O_4/C demonstrates superior ORR/OER performance, which is competitive with commercial Pt/C and RuO_2 for ORR and OER, respectively. Sp-Co_3O_4/C delivers a higher '*j*' value at significantly lower overpotential with greater durability and stability. Sp-Co_3O_4/C favours the ORR with the $4e^-$ pathway, giving a more positive $E_{1/2}$ in comparison to that of C and Co_3O_4/C. The ORR/OER Tafel slope reveals the better kinetics of Sp-Co_3O_4/C as compared to that of Co_3O_4/C and RuO_2.

The superior activity of Sp-Co_3O_4/C is attributed to the synergistic integration of highly exposed Co^{2+} and Co^{3+} active sites of sponge-like Co_3O_4 with C. Moreover, the higher specific surface area of Sp-Co_3O_4/C offers greater space for O_2 adsorption and desorption on the sponge-like Co_3O_4 facilitating enhanced ORR/OER performance. Thus, the comprehensive study offers an aspiring scheme for the fabrication of ORR/OER EC in an alkaline medium with high performance, stability, and durability as cost-effective metal-based ECs.

References

[1] Lewis, N. S., and Nocera, D. G. Powering the planet: Chemical challenges in solar energy utilization. *Proceedings of the National Academy of Sciences*, 103(43):5729-15735, 2006.

[2] Liang, Y., Li, Y., Wang, H., Zhou, J., Wang, J., Regier, T., and Dai, H. Co_3O_4 nanocrystals on graphene as a synergistic catalyst for oxygen reduction reaction. *Nature Materials*, 10(10):780-786, 2011.

[3] Lefèvre, M., Proietti, E., Jaouen, F., and Dodelet, J. P. Iron-based catalysts with improved oxygen reduction activity in polymer electrolyte fuel cells. S*cience*, 324:71-74, 2009.

[4] Liu, Y., Chen, F., Ye, W., Zeng, M., Han, N., Zhao, F., Wang, X. and Li, Y. High-performance oxygen reduction electrocatalyst derived from polydopamine and cobalt supported on carbon nanotubes for metal–air batteries. *Advanced Functional Materials*, 27(12):1606034, 2017.

[5] Liu, X., Park, M., Kim, M. G., Gupta, S., Wu, G., and Cho, J. Integrating NiCo alloys with their oxides as efficient bifunctional cathode catalysts for rechargeable zinc–air batteries. *Angewandte Chemie International Edition*, 54(33):9654-9658, 2015.

[6] Ding, W., Wei, Z., Chen, S., Qi, X., Yang, T., Hu, J., Wang, D., Wan, L.J., Alvi, S.F. and Li, L. Space-confinement-induced synthesis of pyridinic-and pyrrolic-nitrogen-doped graphene for the catalysis of oxygen reduction. *Angewandte Chemie International Edition*, 52:11755-11759, 2013.

[7] Ge, X., Sumboja, A., Wuu, D., An, T., Li, B., Goh, F. T., Hor, T.A., Zong, Y. and Liu, Z. Oxygen reduction in alkaline media: From mechanisms to recent advances of catalysts. *ACS Catalysis*, 5(8):4643-4667, 2015.

[8] Ding, W., Li, L., Xiong, K., Wang, Y., Li, W., Nie, Y., Chen, S., Qi, X. and Wei, Z. Shape fixing via salt recrystallization: A morphology-controlled approach to convert nanostructured polymer to carbon nanomaterial as a highly active catalyst for oxygen reduction reaction. *Journal of the American Chemical Society*, 137(16):5414-5420, 2015.

[9] Guo, S., Zhang, S., Sun, S. Tuning nanoparticle catalysis for the oxygen reduction reaction, *Angewandte Chemie International Edition*, 52:8526-8544, 2013.

[10] Ogbonnaya, C., Abeykoon, C., Nasser, A., and Turan, A. Unitized regenerative proton exchange membrane fuel cell system for renewable power and hydrogen generation: Modelling, simulation, and a case study. *Cleaner Engineering and Technology*, 4:100241, 2021.

[11] Sui, S., Wang, X., Zhou, X., Su, Y., Riffat, S., and Liu, C. J. A comprehensive review of Pt electrocatalysts for the oxygen reduction reaction: Nanostructure, activity, mechanism and carbon support in PEM fuel cells. *Journal of Materials Chemistry A*, 5(5):1808-1825, 2017.

[12] Chen, C., Kang, Y., Huo, Z., Zhu, Z., Huang, W., Xin, H. L., Snyder, J.D., Li, D., Herron, J.A., Mavrikakis, M. and Chi, M. Highly crystalline multimetallic nanoframes with three-dimensional electrocatalytic surfaces. *Science*, 343(6177):1339-1343, 2014.

[13] Wang, Q., Chen, S., Shi, F., Chen, K., Nie, Y., Wang, Y., Wu, R., Li, J., Zhang, Y., Ding, W. and Li, Y. Structural evolution of solid Pt nanoparticles to a hollow PtFe alloy with a Pt-skin surface via space-confined pyrolysis and the nanoscale Kirkendall effect. *Advanced Materials*, 28(48):10673-10678, 2016.

[14] Huang, X., Zhao, Z., Cao, L., Chen, Y., Zhu, E., Lin, Z., Li, M., Yan, A., Zettl, A., Wang, Y.M. and Duan, X. High-performance transition metal–doped Pt_3Ni octahedra for oxygen reduction reaction. *Science*, 348(6240):1230-1234, 2015.

[15] Chen, S., Wei, Z., Qi, X., Dong, L., Guo, Y. G., Wan, L., Shao, Z. and Li, L. Nanostructured polyaniline-decorated Pt/C@PANI core–shell catalyst with enhanced durability and activity. *Journal of the American Chemical Society*, 134(32):13252-13255, 2012.

[16] Kongkanand, A., and Mathias, M. F. The priority and challenge of high-power performance of low-platinum proton-exchange membrane fuel cells. *The Journal of Physical Chemistry Letters*, 7(7):1127-1137, 2016.

[17] Oezaslan, M., and Strasser, P. Activity of dealloyed $PtCo_3$ and $PtCu_3$ nanoparticle electrocatalyst for oxygen reduction reaction in polymer electrolyte membrane fuel cell. *Journal of Power Sources*, 196(12):5240-5249, 2011.

[18] Selvaganesh, S. V., Sridhar, P., Pitchumani, S., and Shukla, A. K. A Durable Graphitic-Carbon Support for Pt and Pt_3Co Cathode Catalysts in Polymer Electrolyte Fuel Cells. *Journal of The Electrochemical Society*, 160(1):F49, 2012.

[19] Zhou, W., Ge, L., Chen, Z. G., Liang, F., Xu, H. Y., Motuzas, J., Julbe, A. and Zhu, Z. Amorphous iron oxide decorated 3D heterostructured electrode for highly efficient oxygen reduction. *Chemistry of Materials*, 23(18):4193-4198, 2011.

[20] Kim, S. W., Lee, H. W., Muralidharan, P., Seo, D. H., Yoon, W. S., Kim, D. K., and Kang, K. Electrochemical performance and ex situ analysis of $ZnMn_2O_4$ nanowires as anode materials for lithium rechargeable batteries. *Nano Research*, 4(5):505-510, 2011.

[21] Roche, I., Chaînet, E., Chatenet, M., and Vondrák, J. Durability of carbon-supported manganese oxide nanoparticles for the oxygen reduction reaction (ORR) in alkaline medium. *Journal of Applied Electrochemistry*, 38(9):1195-1201, 2008.

[22] Chutia, B., and Bharali, P. Oxygen deficient interfacial effect in CeO_2-modified Fe_2O_3/C for oxygen reduction reaction in alkaline electrolyte. *Catalysis Communications*, 164:106432, 2022.

[23] Lian, J., Zhao, J. Y., and Wang, X. M. Recent progress in carbon-based materials of non-noble metal catalysts for ORR in acidic environment. *Acta Metallurgica Sinica (English Letters)*, 34(7):885-899, 2021.

[24] Shahid, M. M., Rameshkumar, P., Basirun, W. J., Juan, J. C., and Huang, N. M. Cobalt oxide nanocubes interleaved reduced graphene oxide as an efficient electrocatalyst for oxygen reduction reaction in alkaline medium. *Electrochimica Acta*, 237:61-68, 2017.

[25] Seh, Z. W., Kibsgaard, J., Dickens, C. F., Chorkendorff, I. B., Nørskov, J. K., and Jaramillo, T. F. Combining theory and experiment in electrocatalysis: Insights into materials design. *Science*, 355(6321):eaad4998, 2017.

[26] Jia, Y., Jiang, K., Wang, H., and Yao, X. The role of defect sites in nanomaterials for electrocatalytic energy conversion. *Chem*, 5(6):1371-1397, 2019.

[27] Zhao, R., Li, Q., Jiang, X., Huang, S., Fu, G., and Lee, J. M. Interface engineering in transition metal-based heterostructures for oxygen electrocatalysis. *Materials Chemistry Frontiers*, 5(3):1033-1059, 2021.

[28] Ahmed, M. S., Choi, B., and Kim, Y. B. Development of highly active bifunctional electrocatalyst using Co_3O_4 on carbon nanotubes for oxygen reduction and oxygen evolution. *Scientific Reports*, 8(1):1-10, 2018.

[29] Odedairo, T., Yan, X., Ma, J., Jiao, Y., Yao, X., Du, A., and Zhu, Z. Nanosheets Co_3O_4 interleaved with graphene for highly efficient oxygen reduction. *ACS Applied Materials & Interfaces*, 7(38):21373-21380, 2015.

[30] Ning, R., Tian, J., Asiri, A. M., Qusti, A. H., Al-Youbi, A. O., and Sun, X. Spinel $CuCo_2O_4$ nanoparticles supported on N-doped reduced graphene oxide: a highly active and stable hybrid electrocatalyst for the oxygen reduction reaction. *Langmuir*, 29(43);13146-13151, 2013.

[31] Liang, Y., Wang, H., Zhou, J., Li, Y., Wang, J., Regier, T., and Dai, H. Covalent hybrid of spinel manganese–cobalt oxide and graphene as advanced oxygen reduction electrocatalysts. *Journal of the American Chemical Society*, 134(7):3517-3523, 2012.

[32] Lin, Q., Liu, B., Jiang, F., Fang, X., Xu, Y., and Liu, X. Assessing the formation of cobalt carbide and its catalytic performance under realistic reaction conditions and tuning product selectivity in a cobalt-based FTS reaction. *Catalysis Science & Technology,* 9(12):3238-3258, 2019.

[33] Chutia, B., Hussain, N., Puzari, P., Jampaiah, D., Bhargava, S. K., Matus, E. V., Ismagilov, I.Z., Kerzhentsev, M. and Bharali, P. Unraveling the role of CeO_2 in stabilization of multivalent Mn species on α-MnO_2/Mn_3O_4/CeO_2/C surface for enhanced electrocatalysis. *Energy & Fuels,* 35(13):10756-10769, 2021.

[34] Jiang, B., Zhao, L., Guo, J., Yan, X., Ding, D., Zhu, C., Huang, Y. and Guo, Z. Improved thermal stability of methyl silicone resins by compositing with N-doped graphene oxide/Co_3O_4 nanoparticles. *Journal of Nanoparticle Research*, 18(6):145, 2016.

[35] Zhang, T., He, C., Sun, F., Ding, Y., Wang, M., Peng, L., Wang, J. and Lin, Y. Co3O4 nanoparticles anchored on nitrogen-doped reduced graphene oxide as a multifunctional catalyst for H_2O_2 reduction, oxygen reduction and evolution reaction. *Scientific Reports*, 7:43638, 2017.

[36] Diallo, A., Beye, A. C., Doyle, T. B., Park, E., and Maaza, M. Green synthesis of Co_3O_4 nanoparticles via Aspalathus linearis: physical properties. *Green Chemistry Letters and Reviews*, 8(3-4):30-36, 2015.

[37] Reddy, K. P., Jain, R., Ghosalya, M. K., and Gopinath, C. S. Metallic cobalt to spinel Co_3O_4-electronic structure evolution by near-ambient pressure photoelectron spectroscopy. *The Journal of Physical Chemistry C*, 121(39):21472-21481, 2017.

[38] Wang, X., Li, X., Mu, J., Fan, S., Chen, X., Wang, L., Yin, Z., Tade, M. and Liu, S. Oxygen vacancy-rich porous Co_3O_4 nanosheets toward boosted NO reduction by CO and CO oxidation: Insights into the structure-activity relationship and performance enhancement mechanism. *ACS Applied Materials & Interfaces*, 11(45):41988-41999, 2019.

[39] Hadjiev, V. G., Iliev, M. N., and Vergilov, I. V. The Raman spectra of Co_3O_4. *Journal of Physics C: Solid State Physics*, 21(7):L199, 1988.

[40] Patowary, S., Chetry, R., Goswami, C., Chutia, B., and Bharali, P. Oxygen reduction reaction catalysed by supported nanoparticles: Advancements and challenges. *ChemCatChem*, 14(7):e202101472, 2022.

[41] Goswami, C., Hazarika, K. K., Yamada, Y., and Bharali, P. Nonprecious hybrid metal oxide for bifunctional oxygen electrodes: Endorsing the role of interfaces in electrocatalytic enhancement. *Energy & Fuels*, 35(16):13370-13381, 2021.

[42] Wang, Z., Wang, W., Zhang, L., and Jiang, D. Surface oxygen vacancies on Co_3O_4 mediated catalytic formaldehyde oxidation at room temperature. *Catalysis Science & Technology*, 6(11):3845-3853, 2016.

[43] Si, J., Xiao, S., Wang, Y., Zhu, L., Xia, X., Huang, Z., and Gao, Y. Sub-nanometer Co_3O_4 clusters anchored on TiO_2 (B) nano-sheets: Pt replaceable Co-catalysts for H_2 evolution. *Nanoscale,* 10(5):2596-2602, 2018.

[44] Lu, X. F., Wu, D. J., Li, R. Z., Li, Q., Ye, S. H., Tong, Y. X., and Li, G. R. Hierarchical $NiCo_2O_4$ nanosheets@ hollow microrod arrays for high-performance asymmetric supercapacitors. *Journal of Materials Chemistry A*, 2(13):4706-4713, 2014.

[45] Budiyanto, E., Yu, M., Chen, M., DeBeer, S., Rüdiger, O., and Tüysüz, H. Tailoring morphology and electronic structure of cobalt iron oxide nanowires for electrochemical oxygen evolution reaction. *ACS Applied Energy Materials*, 3(9):8583-8594, 2020.

[46] Rao, B. G., Sudarsanam, P., Rao, T. V., Amin, M. H., Bhargava, S. K., and Reddy, B. M. Highly dispersed MnO_x nanoparticles on shape-controlled SiO_2 spheres for eco-friendly selective allylic oxidation of cyclohexene. *Catalysis Letters*, 150(10):3023-3035, 2020.

[47] Fink, M. F., Eckhardt, J., Khadke, P., Gerdes, T., and Roth, C. Bifunctional α-MnO_2 and Co_3O_4 catalyst for oxygen electrocatalysis in alkaline Solution. *ChemElectroChem*, 7(23):4822-4836, 2020.

[48] Goswami, C., Yamada, Y., Matus, E. V., Ismagilov, I. Z., Kerzhentsev, M., and Bharali, P. Elucidating the role of oxide-oxide/carbon interfaces of CuO_x-CeO_2/C in boosting electrocatalytic performance. *Langmuir*, 36(49): 15141-15152, 2020.

[49] Huang, Y., Zhang, M., Liu, P., Cheng, F., and Wang, L. Co_3O_4 supported on N, P-doped carbon as a bifunctional electrocatalyst for oxygen reduction and evolution reactions. *Chinese Journal of Catalysis,* 37(8):1249-1256, 2016.

[50] Wang, Q., Hu, W. H., and Huang, Y. M. One-pot synthesis of Co/Co_3O_4/$Co(OH)_2$/N-doped mesoporous carbon for both oxygen reduction reactions and oxygen evolution reactions. *ChemistrySelect,* 2(10):3191-3199, 2017.

[51] Wang, Q., Hu, W., and Huang, Y. Nitrogen doped graphene anchored cobalt oxides efficiently bi-functionally catalyze both oxygen reduction reaction and oxygen evolution reaction. *International Journal of Hydrogen Energy*, 42(9):5899-5907, 2017.

[52] Han, X., He, G., He, Y., Zhang, J., Zheng, X., Li, L., Zhong, C., Hu, W., Deng, Y. and Ma, T.Y. Engineering catalytic active sites on cobalt oxide surface for enhanced oxygen electrocatalysis. *Advanced Energy Materials*, 8(10):1702222, 2018.

[53] Niu, Y., Huang, X., Zhao, L., Hu, W., Li, C. M. One-pot synthesis of Co/$CoFe_2O_4$ nanoparticles supported on N-doped graphene for efficient bifunctional oxygen electrocatalysis. *ACS Sustainable Chemistry & Engineering*, 6(3):3556-3564, 2018.

[54] Wang, D., Chen, X., Evans, D. G., and Yang, W. Well-dispersed Co_3O_4/Co_2MnO_4 nanocomposites as a synergistic bifunctional catalyst for oxygen reduction and oxygen evolution reactions. *Nanoscale*, 5(12):5312-5315, 2013.

[55] Hu, T., Wang, Y., Zhang, L., Tang, T., Xiao, H., Chen, W., Zhao, M., Jia, J. and Zhu, H. Facile synthesis of PdO-doped Co_3O_4 nanoparticles as an efficient bifunctional oxygen electrocatalyst. *Applied Catalysis B: Environmental*, 243:175-182, 2019.

[56] Zhu, Y., Liu, X., Jin, S., Chen, H., Lee, W., Liu, M., and Chen, Y. Anionic defect engineering of transition metal oxides for oxygen reduction and evolution reactions. *Journal of Materials Chemistry A*, 7(11):5875-5897, 2019.

[57] Xu, L., Jiang, Q.; Xiao, Z.; Li, X., Huo, J.; Wang, S., and Dai, L. Plasma-engraved Co_3O_4 nanosheets with oxygen vacancies and high surface area for the oxygen evolution reaction. *Angewandte Chemie International Edition,* 55*:*5277–5281, 2016.

[58] Zhuang, L., Ge, L., Yang, Y., Li, M., Jia, Y., Yao, X., and Zhu, Z. Ultrathin iron-cobalt oxide nanosheets with abundant oxygen vacancies for the oxygen evolution reaction. *Advanced Materials*, 29(17):1606793, 2017.

[59] Liu, Z., Wang, G., Zhu, X., Wang, Y., Zou, Y., Zang, S., and Wang, S. Optimal geometrical configuration of cobalt cations in spinel oxides to promote oxygen evolution reaction. *Angewandte Chemie International Edition*, 59:4736-4742, 2020.